Experimental Thermal and Fluid Science 163 (2025) 111395

Contents lists available at ScienceDirect

Experimental Thermal and Fluid Science

journal homepage: www.elsevier.com/locate/etfs

Measurements of the unsteady wall shear stress vector using multi-aperture defocusing microscopic particle tracking velocimetry

Joachim Klinner *, Christian E. Willert

DLR Institute of Propulsion Technology, German Aerospace Center, Köln, 51170, Germany

ARTICLE INFO

Keywords:
Fluid flow measurement
Turbulent boundary layer
Wall shear stress
Coded aperture imaging
Particle tracking
PTV

ABSTRACT

A volumetric, three component microscopic particle tracking velocimetry (μPTV) system is presented which relies on single window optical access for both high-speed tracer illumination and image recording. Similar to the triple aperture "defocusing" concept originally introduced by Willert and Gharib (1992), the wall distance of individual particles is obtained from the size of projected particle image triplets formed by a triplet of apertures on the entrance pupil of the microscope lens. The measurement principle is validated with particle tracking measurements of a canonical turbulent boundary layer (TBL) within the closed test section of a wind tunnel at free-stream velocities of $5.2 \leq U_\infty \leq 20\,\mathrm{m/s}$ with corresponding shear Reynolds numbers of $560 \leq \mathrm{Re}_\tau \leq 1630$. Velocity profiles and higher order statistics are obtained by bin averaging of the particle velocity data up to the inner turbulence peak at a wall distance of $y^+ = \nu/u_\tau \approx 15$ with a spatial resolution better than 5 μm. Excellent agreement with DNS data was obtained at similar Reynolds numbers. The unsteady wall shear stress (WSS) is estimated from particle tracking data sampled in the viscous sub-layer ($y^+ \leq 4$). The joint probability density distributions of stream- and spanwise WSS components are reliably obtained down to probability densities of 10^{-3} which, to date, has rarely been achieved through measurements. Fluctuations of the WSS components follow the Reynolds number dependency of the correlations reported in the literature but were found to be systematically underestimated with increasing distance of the sampling volume from the wall, affecting the spanwise component to a higher degree. A correction method is suggested.

1. Introduction

Measurement techniques capable of measuring the two-component (2c) fluctuating wall shear stress field on submerged bodies are of great importance to improve the physical understanding of wall-bounded turbulent flows, the details of flow separation, the mechanisms governing viscous drag and convective heat transfer and structural vibrations in several engineering applications including aviation, shipping and land vehicles. In general, the viscous skin friction is related to the stream- and spanwise characteristics of the wall shear stress (WSS) vector $\vec{\tau}_w$. This quantity is directly related to the flow dynamics in the viscous sublayer in the immediate proximity of the no-slip surface and can be estimated from tracer particle's velocity **u** and its distance from the wall y through the relation:

$$\vec{\tau}_w = \mu \left.\frac{\partial \mathbf{u}}{\partial y}\right|_{y=0} = \mu \lim_{y\to 0} \frac{\mathbf{u}(y)}{y} \approx \mu \frac{\mathbf{u}(\Delta y)}{\Delta y} \tag{1}$$

with x, y, z being the streamwise, wall-normal and spanwise coordinates and with μ the dynamic viscosity of the fluid. In the following, the superscript (+) denotes viscous scaling where the length unit is defined as $l^* = \nu/u_\tau$, with ν being the kinematic viscosity and $u_\tau = \sqrt{\langle \tau_w \rangle/\rho}$ the friction velocity of the boundary layer flow. In particular, l^* and u_τ are essential scaling parameters of mean and fluctuating velocity profiles in turbulent boundary layers (TBL). With respect to the organization of near-wall structures of turbulent wall-bounded flows and its interaction with the larger structures from the outer layer, the positively skewed, streamwise wall shear stress distribution and its so-called near-wall events, i.e. *reverse flow events* or *extreme positive events*, have received increased attention as they are indicators of the high intermittency of the WSS, which in turn has impact on the mixed scaling in the wall-attached eddies range when modeling wall-bounded flows [1–4]. In addition, numerical simulations indicate that fluctuations, skewness and flatness of the WSS distribution exhibit a friction Reynolds number dependency, which is still a subject of scientific discussion, in part, because the experimental database is limited, especially with regard to the spanwise component $\tau_{w,z}$ [2,5–7].

Very few measurement techniques capable of measuring the unsteady WSS directly are reported in literature (see review by [8] on various approaches). Gnanamanickam et al. [9] characterized and

* Corresponding author.
E-mail address: joachim.klinner@dlr.de (J. Klinner).

https://doi.org/10.1016/j.expthermflusci.2024.111395
Received 7 October 2024; Received in revised form 2 December 2024; Accepted 12 December 2024
Available online 19 December 2024

Nomenclature

F	Flatness or kurtosis [-]
N_s	Number of samples [-]
S	Skewness or similarity [-]
$\vec{a}$	Triplet side vector [pixel]
$\vec{e}$	Triplet reference vector [pixel]
d	Diameter [mm]
f	Focal length [mm]
f_s	Sampling frequency [s^{-1}]
l^*	Viscous length unit $\nu\, u_\tau^{-1}$ [μm]
m	Magnification [-]
u, v, w	Velocity components in x, y, z [m/s]
u_∞	Free stream velocity [m/s]
u_τ	Friction velocity $(\langle\tau_x\rangle\rho^{-1})^{0.5}$ [m/s]
u_e	BL edge velocity [m/s]
x	Streamwise coordinate [mm]
y	Wall-normal coordinate [mm]
z	Spanwise coordinate [mm]

Acronyms

BL	Boundary layer
DNS	Direct numerical simulation
LES	Large-eddy simulation
MA-μPTV	Multi-aperture micro PTV
PDF	Probability density function
PIV	Particle image velocimetry
PTV	Particle tracking velocimetry
rms	Root mean square
SE	Standard error
SPIV	Stereoscopic PIV
TBL	Turbulent BL
WSS	Wall shear stress
ZPG	Zero pressure gradient

Dimensionless values

Re_τ	Friction Reynolds number $u_\tau\, \delta_{99}\, \nu^{-1}$
Re_θ	Reynolds number $u_\infty\, \theta\, \nu^{-1}$
Stk	Particle Stokes number $t_p\, t_\eta^{-1}$

Greek symbols

δ	Disparity of particle position [μm]
δ_{99}	BL thickness at $0.99\, u_e$ [mm]
ϵ	Relative error [%]
μ	Dynamic viscosity [Pa s]
ν	Kinematic viscosity [$m^2\, s^{-1}$]
θ	Momentum thickness [μm]
$\vec{\tau}_w$	WSS vector [Pa]
τ_x	WSS, streamwise component (= $\tau_{w,x}$) [Pa]
τ_z	WSS, spanwise component (= $\tau_{w,z}$) [Pa]

Superscripts and subscripts

$'$	Centered by the mean value
$+$	Viscous scaling using l^*, u_τ
0	Wall position
p	Particle related

dynamically calibrated micro-pillars which were later used by Liu et al. [10] to obtain unsteady maps of both the stream- and spanwise WSS. The authors stated that the underestimation of the fluctuations $\tau_{x,\mathrm{rms}}$ and $\tau_{z,\mathrm{rms}}$ with respect to the DNS data is related to the averaging effect caused by the pillars' length exceeding the thickness of the viscous sublayer.

Aside from micro pillars which measure the wall shear directly, early micro-electromechanical systems (MEMS) based approaches [11] provided arrays of thermal sensors [12] that can "image" the footprint of the unsteady WSS with a frequency response of 25 kHz allowing to monitor and characterize high shear-stress streaks. Ruedi et al. [13] applied MEMS based thermal sensors for unsteady WSS measurements and found a strong dependence of the unsteady performance of the MEMS on the mean skin friction as well as variations in the angular sensitivity. The authors concluded, that more experiments are required to better identify and understand the influence of different parameters on the MEMS performance.

Alfredsson et al. [14] applied hot-film sensors and hot-wires for characterization of the unsteady WSS. The authors focused on the limiting behavior of the streamwise velocity fluctuations at the wall. Recently, Gubian et al. [6] applied flush mounted hot-wire probes where the hot wire is installed over a small rectangular cavity to investigate the Reynolds number dependence of WSS in a turbulent channel flow up to $\mathrm{Re}_\tau \leq 950$. The results show an asymptotic behavior beyond $\mathrm{Re}_\tau = 600$, which stands in contrast to several direct numerical simulation (DNS) based studies in recent years. On the other hand, the study by Perez et al. [7] identified combining effects of insufficient spatial resolution which lead to an overestimation of fluctuating levels due to influences of the cavity.

In the case of particle-based velocimetry, the unsteady wall shear stress can be estimated from the velocity gradient in the vicinity of the wall as indicated in Eq. (1). This approach requires accurate measurement of two quantities, namely, the instantaneous near-wall velocity $\mathbf{u}$ within the viscous sublayer ($y^+ < 5$) along with the distance y from the wall at which the velocity measurement is obtained. For many laser-based techniques this is very challenging due to laser light reflections in the vicinity of the wall. In addition, with regard to particle image velocimetry (PIV), spatial resolution issues typically impose limitations on capturing strong gradients near the wall.

Numerous single-camera particle velocimetry techniques rely on imaging configurations that restrict the measurement to at most two velocity components, streamwise and wall-normal, which generally leaves the spanwise motions unaccounted for. Measurements of the streamwise WSS fluctuations using PIV and particle tracking velocimetry (PTV) were performed by Li et al. [15] and de Silva et al. [16] but without temporal resolution. high-speed particle image velocimetry (HSPIV) at high image magnification has recently been shown capable of providing instantaneous streamwise wall shear in a ZPG TBL at Re_τ up to 5600 ($u_\tau = 0.34$ m/s) by fitting the unsteady velocity gradient $\partial u/\partial y$ derived from 1d cross-correlation of wall-parallel image rows [17,18]. Beyond mean and fluctuating velocity profiles, which coincide with DNS calculations, the resulting probability density function (PDF) of the WSS indicated occasional reverse flow events, which were confirmed by searching for near-wall velocities in the time-resolved velocity records. Although the streamwise and wall-normal extents of reverse flow regions align with DNS (e.g. [19]), the spanwise extent of these structures remained uncovered with these techniques and require more complex 3d 3c imaging techniques.

On the other hand, the reduced seeding density in the viscous sublayer facilitates the application of 3d particle tracking velocimetry (PTV), which allows the capture of both components of the WSS vector. Although limited to water flows, [20,21] utilized inline digital holography to obtain high magnification flow data and recovered the 2d joint PDFs by PTV, using relatively low hardware complexity with a single high-speed camera and combined optical access for both tracer illumination and imaging. At Re_τ= 400, Kumar et al. [21] were able

to record numerous tracks with strongly meandering spanwise motion and increased acceleration in the viscous sublayer with spans of [2–3] l^*, stating, that to date, there are hardly any experimental studies that allow a quantification of these near-wall spanwise motions by non-intrusive measurements. The measured PDF of the WSS are in good agreement with DNS predictions showing deviations towards the extreme ends, that is, rare reverse flow events and high stress events are underestimated. The authors suspected that the deviations from DNS could be caused by resolution issues that lead to an overestimation of streamwise high stress events and an underestimation of the spanwise stress events.

1.1. Wall shear stress measurement using defocusing approaches

Defocusing techniques as micro particle tracking velocimetry (μPTV) [22] along with astigmatism μPTV [23–25] also have the potential of providing unsteady WSS measurements at low hardware complexity. Fuchs et al. [26] applied defocusing μPTV in the viscous sublayer of a ZPG TBL at $\mathrm{Re}_\tau \leq 8940$ with $u_\tau \leq 1.37\,\mathrm{m/s}$ and evaluated mean and fluctuating velocities up to wall distances of $y^+ = 6$. While mean axial velocities agreed well with the linear region in the viscous sublayer up to $\mathrm{Re}_\tau = 3260$ ($u_\tau = 0.46\,\mathrm{m/s}$), with increasing Re_τ slight underestimation of mean velocities was observed. Diagnostic plots [27] of their data indicated an overestimation of fluctuating velocities near the wall. The authors concluded that defocusing μPTV is a feasible concept for the measurement of the mean WSS but suffers from increasing uncertainties of particle positions with increasing wall distance.

In the following, we will present a defocusing measurement system based on 3d 3c micro PTV that is capable of simultaneously providing unsteady measurements of both components of the wall shear stress (WSS) vector. The instrument is based on a single high-speed camera and a microscope lens along with a high-speed laser (Fig. 1) for particle illumination. Within the microscope lens a mask with a triplet of apertures implements a depth-from-defocus concept as initially introduced by [28], an imaging configuration that is also known as *aperture encoded imaging*. The depth encoding is based on the separation of multiple images of the same particle, generated by different – in this case three – beam paths through a pinhole mask placed in the lens pupil. Herein, these self-similar particle image triplets will be referred to as *triplets*. To avoid confusion with *defocusing* μPTV, the term multi-aperture microscopic particle tracking velocimetry (MA-μPTV) is used to describe the herein introduced measurement technique.

Since its introduction by [28], the"defocusing concept" shifted towards the use of multiple cameras for applications at macroscopic scale to avoid increased crowding of the detector at higher particle densities and to increase the depth sensitivity by increasing the separation of the individual "apertures" (see e.g. 29,30). On the other hand, single lens configurations typically have been used in microscopic imaging applications [31–33].

Using the simplified geometric analysis as provided in [28,30], the depth sensitivity of a microscopic setup can be predicted for different pinhole separations. For example, for a typical long working distance microscope objective with magnification of 5× and at a typical pixel pitch for high-speed cameras of 13.5 μm, a nearly constant sensitivity of $72\,\mathrm{pixel\,mm^{-1}}$ can be achieved for a measurement volume of 0.5 mm depth if the pinhole spacing fully utilizes the diameter of the entrance pupil. Assuming that the triplet size can be detected with sub-pixel accuracy of 0.5 pixel, such a sensitivity would be sufficient to achieve an accuracy in y of 6 μm, which we found promising. Another aspect is that small pinhole diameters result in a reduced beam divergence compared to defocusing PTV, and thus to a lower particle image broadening over depth, albeit at proportionally reduced particle image intensities at f-numbers exceeding 20 (i.e. focal length of the microscope objective divided by the pinhole diameter).

Yoon and Kim [31] applied the multiple pinhole technique in microfluidics using a microscopic objective with $m = 20$ and pinholes with 1.5 mm diameter. Cierpka et al. [24] estimated the ratio of peak image intensity to noise floor to be one order of magnitude lower for MA-μPTV in comparison to astigmatism μPTV for such an imaging configuration. On the other hand, using this microscopic setup Yoon and Kim [31] successfully applied MA-μPTV to a backward facing step and quantified the root mean square (rms) of the depth position to be in the order of 0.2 pixel at a depth sensitivity of $1.2\,\mathrm{\mu m\,pixel^{-1}}$. Also, the authors observed a non-linearity of the depth sensitivity and noticed that each vertex of the triangular image pattern increases at different rate with depth and image position, which originates from deviations from self-similarities of triplet images, even though the three pinholes have an equilateral arrangement. The authors compensated for this non-linearity by applying polynomial calibration functions that depend on the image coordinates and also introduced a similarity parameter to distinguish overlapping particle images.

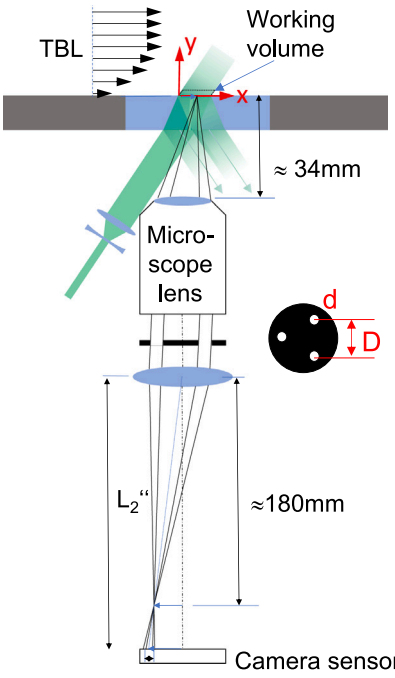

Fig. 1. Optical arrangement for MA-μPTV for boundary layer measurements using single window access.

In our previous work, the feasibility of MA-μPTV for WSS measurements was demonstrated in a developing turbulent duct flow of a small wind tunnel up to $\mathrm{Re}_\tau = 836$ [34]. The present contribution extends upon the previously published material by applying MA-μPTV on a well-characterized TBL to track the near-wall motion of tracer particles with the aim of estimating the unsteady WSS from the particles' velocity and comparing the data with DNS results from literature.

The paper is organized as follows: After a description of the measurement setup and calibration, the image processing, including triplet matching and particle tracking, as well as the procedure for the exact determination of the wall position are explained. This is followed by an error assessment. The results section focuses mostly on bin averaged profiles that are obtained from the ensemble of particle tracks, yielding near-wall flow statistics and derived WSS distributions, and discusses the results in reference to the data from the DNS as well as shortcomings and limitations of the technique presented herein.

2. Measurement setup

2.1. Multi-aperture micro-PTV system and wind tunnel facility

All measurements are performed on the closed test section of the 1 m wind tunnel of DLR in Göttingen (1mWK) at free-stream velocities

of 5.2 m/s $\leq u_\infty \leq$ 20 m/s with corresponding shear Reynolds numbers of 560 $\leq \mathrm{Re}_\tau \leq$ 1630 and friction velocities 0.22 m/s $\leq u_\tau \leq$ 0.74 m/s. As shown in Fig. 2(a), the high-speed camera (Vision Research V2640) and an infinity corrected microscope lens (Mitotuyo Plan Apo 5×, $f = 40$ mm) are placed below the test section. Since the measurement volume is imaged directly through the glass wall, issues that would normally arise with side-viewing configurations such as parallax and perspective errors due to the slight oblique viewing angle [35] are mitigated in the present configuration.

The microscope objective is combined with a microscope tube lens of $f = 180$ mm which results in an effective magnification of 4.5×. The pinhole mask consists of a black anodized aluminum foil which is located in the nearly parallel optical path between the objective and the tube lens (cf. Fig. 1). The mask contains three precision-milled pinholes each with a diameter 2 mm that form an equilateral triangle. The spacing between the pinholes D is maximized such that the apertures fall just inside the entrance pupil diameter $d_{ep} = 11.2$ mm of the objective. The ratio between in-plane and depth resolution is 5.05 and corresponds approximately to the ratio of the focal length of the microscope lens divided by the pinhole spacing thereby confirming relations also provided by Willert and Gharib [28]. The collimated beam from two high-speed pulsed lasers (2× Innolas Photonics Nanio Air) is introduced at an angle of about 30° through the same flush-mounted, anti-reflection coated window in the wind tunnel wall. Both lasers have an average rated power of 10 W at a pulse repetition rate of 40 kHz and fire simultaneously, providing ≈ 0.5 mJ per pulse. A beam expander is used to increase the beam diameter to roughly 2.3 mm to enable illumination of the entire measurement volume (cf. Fig. 2). The oblique laser incidence was chosen to prevent direct back reflections of the laser light from the window into the objective, thus reducing the risk of damage to the camera sensor.

Within the wind tunnel, the TBL is tripped about 1.5 m upstream of the measurement location allowing it to grow to a thickness of about 35 mm. The flow is seeded with $d_p = [1-2]$ µm aerosol droplets from a water-based fog generator (HazeBase Classic, base*M fluid). For the present experiment, Willert and Klinner [36] assessed the particle response behavior and estimated the particle relaxation time with 3 µs $< t_p <$ 12 µs for the given droplet sizes range. Provided that the characteristic time scale in the viscous sublayer is the Kolmogorov time scale $t_\eta = \nu/u_\tau^2$, the particle Stokes-number can be calculated by $\mathrm{Stk} = t_p t_\eta^{-1}$ such that Stk ≤ 0.04 at $U_\infty = 5.2$ m/s ($t_\eta \approx 165$ µs). At $U_\infty = 10$ m/s the Kolmogorov time scale decreases to $t_\eta \approx 100$ µs with Stk ≤ 0.12. At the highest velocity of $U_\infty = 20.0$ m/s and $t_\eta \approx 28$ µs the Stokes number further increases to Stk $= 0.44$ for particles with $d_p = 2$ µm. Even at the highest velocities, the particle Stokes number is well below unity and particles are considered to be well-tracked by the fluid flow, meaning that they will follow the flow accurately.

To match the free-stream velocity, the framing rate of the high-speed camera is varied between 20 kHz and 37 kHz with a field of view of 640 × 480 pixel or 768 × 360 pixel in stream- and spanwise direction, respectively. Per condition up to 16 sequences of 39 000 to 51 000 images constitute the basis for the subsequent 3D-PTV processing. Table 1 provides an overview on test points for which sequences were acquired with MA-µPTV.

3. Triplet image characteristics and calibration

Fig. 3 highlights some peculiarities of recorded triplet images (see also the image sequences provided as supplementary material). In comparison to images aquired for profile PIV, the MA-µPTV images are sparsely populated with particles due to the relatively small streamwise image extent of 1.8 mm at a magnification that is 4–5× larger in comparison to profile PIV (see Appendix C).

On the other hand, the reduced particle image density is in fact beneficial for PTV as it improves the triplet matching probability.

Table 1
Overview on the dataset acquired with MA-µPTV at the 1 m low-speed wind tunnel (1mWK) at the DLR Göttingen; outer BL parameters are obtained from high-speed profile PIV measurements at similar conditions.

u_∞ [m/s]	5.2	7.5	10.0	15.0	20.0
u_e [m/s]	5.25	7.57	10.17	15.21	20.29
δ_{99} [mm]	38.75	38.12	36.84	34.50	34.37
Re_θ	1573	2265	2895	4009	5227
f_s [kHz]	20; 28	28	28; 37	37	37
Samples	16 × 38 888	16 × 38 888	16 × 51 372	16 × 51 372	16 × 45 228
image sz. [pixel]	640 × 480	640 × 480	640 × 360	640 × 360	768 × 360
image sz. [mm^2]	1.86 × 1.40	1.86 × 1.40	1.86 × 1.05	1.86 × 1.05	2.23 × 1.05

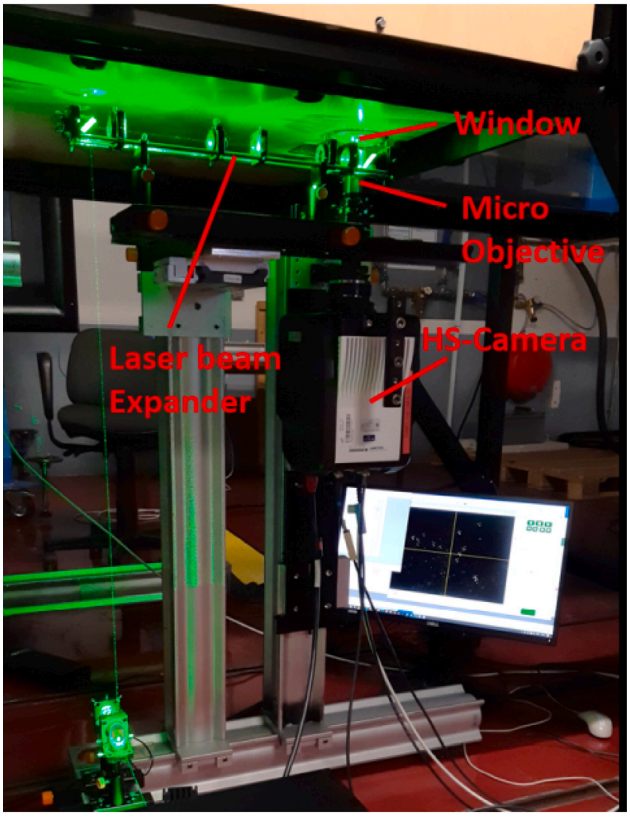

Fig. 2. Photograph of the optical setup for MA-µPTV below the test section of the 1mWK at DLR Göttingen.

Inspecting Fig. 3(a), it can be observed that for a given wall distance, the particle images exhibit very different brightness levels, typically 1.5–20× larger than the average background intensity. A reason for this is the varying scattering behavior of tracer particles depending on their size along with variations in the irradiance of the obliquely incident Gaussian laser beams. In addition, the vertices of a single triplet can vary in brightness and width due to the inhomogeneous scattering behavior of the liquid droplets combined with the coherent nature of the laser light source (Mie scattering). The images at the vertices of the particle image triplets have relatively large diameters of around six pixels, with a minor variation in size across the depth of field of 0.8 mm. Since the pinhole mask blocks most of the light back-scattered by the tracers, some of the image intensities are close to the background intensity level which necessitates the specific image processing, as described in the following section.

To obtain the triangular shape and orientation at various depth positions, a calibration procedure was conducted using a lithographically manufactured dot grid on a glass substrate, with the glass surface aligned nearly parallel to the bottom wall of the wind tunnel. The dot diameter was 5 µm at an equilateral spacing of 150 µm along x and

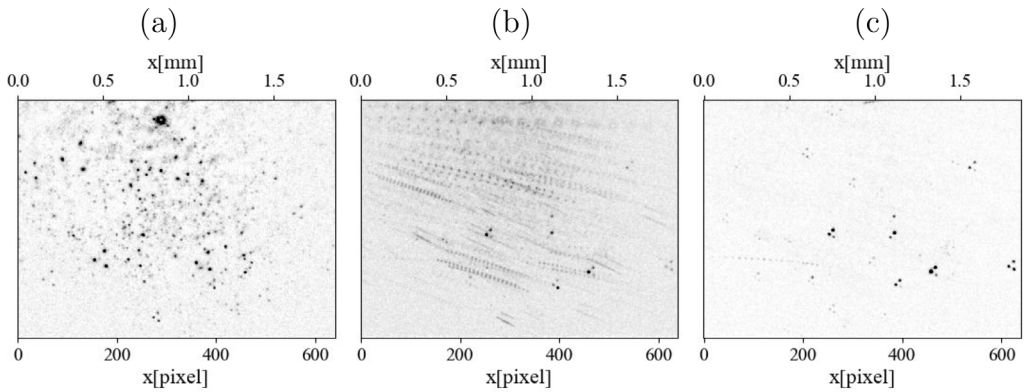

Fig. 3. (a) MA-μPTV sample image recorded in the turbulent boundary layer at $Re_\tau = 754$ (b) composite image showing particle tracks obtained by overlaying 20 successive recordings acquired at 28 kHz (c) minimum image showing only stationary particles (mean flow is from left to right).

z. The glass plate was back-lit with a green LED and traversed by a small motorized translation stage. The translation stage was driven by a piezo motor in closed loop operation with position feedback by a linear encoder (accuracy of 0.2 μm).

Fig. 4 shows composite images of calibration images of triplets in different image corners at different wall distances y. Dot image centers were obtained by a 2d Gaussian fit. With respect to a reference triangle $\vec{e}_1, \vec{e}_2, \vec{e}_3$ determined at the measurement volume center, in each image corner the triplets $\vec{a}_1, \vec{a}_2, \vec{a}_3$ not only vary in size but also are slightly skewed and deviate from self-similarity with respect to the reference triangle at the center. To emphasize this point, the maximum angular deviation with respect to the three sides are also provided in the Fig. 4. Although the pinholes were arranged as equilateral triangles, the reference triplet (cf. Fig. 4, center) also exhibits differences among the triangle's edge lengths. In addition the particle's position estimate determined from the triangle's centroid (i.e. the mean of vertices) does not coincide across the depth of field showing deviations along y of [1.74–3.7] pixel mm^{-1}. Applying the definition of particle position by [31] using the circumcenter of the triangle led to a slightly higher scattering of deviations in the range [1.47–5.07] pixel mm^{-1}.

Deviations of the triplet images from an equilateral pinhole shape were already observed by Yoon and Kim [31]. As possible causes the authors suggested imperfections of the pinhole mask and its de-centering with respect to the lens. In the present experiment, it was also observed that the de-centering between the rigid tube system – consisting of microscope lens, pinhole mask and tube lens – and the camera sensor also is a significant factor. This de-centering was compensated as best as possible by translating the tube lens system laterally to the sensor. Remaining imperfections and triplet distortions were compensated using a set of calibration parameters that will be described in the following.

To quantify deviations from self-similarity and to assign triplet images from neighboring dot images we use the similarity parameter S, defined as:

$$S = Min\left\{ \frac{\vec{a}_i \cdot \vec{e}_i}{\|\vec{a}_i\| \, \|\vec{e}_i\|} \right\}_{i=1,2,3} \tag{2}$$

Fig. 5(a) indicates the range of S of triplet images in different image regions when at each node the triplet nearest to the wall serves as reference. The deviations in S are evident because the direction of the sides $\vec{e}_1, \vec{e}_2, \vec{e}_3$ is not constant, as shown in Fig. 5(b) for $\vec{e}_1$. Here it was found that the direction varies non-linearly with both the image position and the wall distance, which is accounted for by a second order polynomial fit.

Since the matching of particle images belonging to the same triplet is based on the similarity with respect to the reference triplet $\vec{e}_1, \vec{e}_2, \vec{e}_3$, whose shape depends on the position x, y, z, these reference vectors are finally obtained from a second order polynomial over y, for which the three parameters are linearly interpolated over x and z. In total 9 parameters are used. The resulting curves are shown by the dashed lines in Fig. 5(b) which exhibit the largest biases in the top right and bottom left image corner. These deviations were found to be acceptable within the tolerated similarity of $S > 0.998$.

Fig. 5(c) indicates a constant slope of the separation gradient $\partial b_{AB}/\partial y$ which increases proportionally with the depth position but exhibits a varying offset between [18–22] pixel corresponding to an offset of about $y_0 = 190$ μm to the focal point. The reason for this is an offset between the calibration plate and the wall and that the position at which the triplets converge to a point has been chosen within the glass in order to have triplets with similar orientation in the wall-bounded measurement volume. Variation of the offset with the image position indicates a slight tilt between the calibration plate and the focal plane, which is compensated by fitting the wall position y_0 using images of particles that are stuck to the wall, as will be described later.

Fig. 5(d) indicates variations of the magnification within the measurement volume evaluated through the mean spacing of triplet centers at the nodes of the calibration plate. The triplet center (i.e. particle's position) was either evaluated using the centroid or the circumcenter of the three vertices. Again, positions of the grid spacing evaluated by the triplet's centroid provides less scattering compared to the circumcenter. Pincushion or barrel distortion effects could not be detected with the optical configuration used, as indicated by the small rms from the mean magnification per calibration plane of maximum ±0.2%.

Fig. 5(d) exhibits an increasing magnification with the wall-distance y which is contradictory to imaging with a single convex lens where the magnification always decreases with increasing object distance. This deviation is related to the two-stage imaging and is explained in more detail in Appendix B.

4. Triplet image processing

In order to minimize the distortions through window contamination by particle deposition, a sliding minimum over 20 frames is subtracted from each image. In a further step, particle images are identified by segmentation for which each image is convolved with a Gaussian template of $\sigma = 1.8$ pixel and 8 pixel × 8 pixel size. Potential particle images were identified for regions exceeding a given threshold of the normalized cross-correlation coefficient. Image regions segmented in this way were filtered to exclude regions covering an area smaller than a certain threshold, i.e. 6 pixels, since these regions were primarily associated with noise. For the remaining particle image regions the centroids are determined. To map the particle images into triplets (i.e. triplet matching), a search is performed on the centers to find particle image pairs that belong to the same triplet. Matching is based on the similarity S when comparing $\vec{a}_1$ with the reference vector $\vec{e}_1(x, y, z)$ for which the latter is provided through a look-up-table based on the calibration

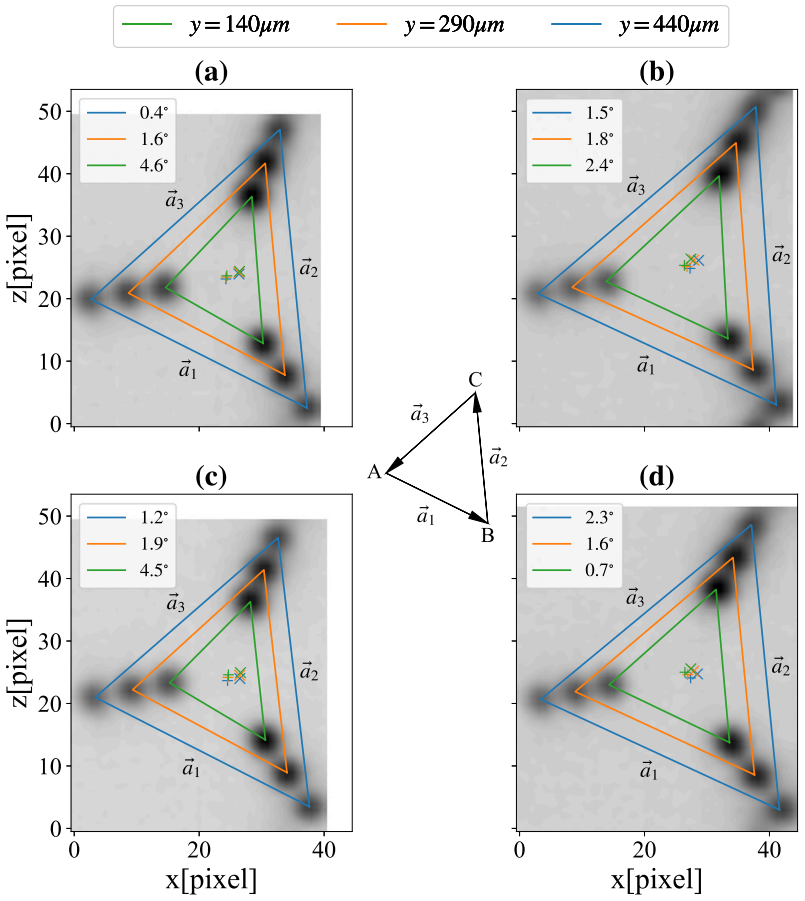

Fig. 4. Composite images of calibration images taken at different wall distances y and at the (a) top left (b) top right (c) bottom left (d) bottom right image corners including the maximum angular deviations from reference triangle sides; + : particle position by a center of mass; ×: particle position by center of the circumcircle.

data. For particle image pairs above a certain threshold, a search for the neighboring particle images $\vec{a}_2$, $\vec{a}_3$ that maximize the similarity of the triplet is performed. Once a triplet is identified, the three particle image centers are refined by means of least squares fitting of a 2d Gaussian of predetermined width. The depth position is obtained by the mean of y_1, y_2 and y_3 using the calibration curves Fig. 5(c) for the vertices $\|\vec{a}_1\|$, $\|\vec{a}_2\|$ and $\|\vec{a}_3\|$. Since a depth position can be determined for each side of the triangle, the half of the maximum absolute deviation between the three positions serves as measure of reconstruction quality δy (i.e. disparity).

To increase the yield for partially overlapping triplet images, the procedure is repeated once on the residual image which is obtained by subtracting the fitted Gaussian distributions.

To obtain estimates of the width of noisy particle images, a set of images was pre-processed in the manner described above with details provided in [34]. The particle images are accumulated separately for each corner (A, B, C) in $8 \times 8 \times 10$ adjacent spatial bins of $233\,\mu m^3 \times 233\,\mu m^3 \times 291\,\mu m^3$ size along x, y, z. This is implemented by shifting the particle images to a uniform position within windows of $12\,\text{pixel} \times 12\,\text{pixel}$ using third order spline interpolation.

Fig. 6 shows a sample image processed as described above with (b) and (c) showing the residual images after the first and second iteration. The centers of the particle images resulting from the triplet matching are indicated by circles with color-coding indicating the wall distance. Some skewed triplets can clearly be observed with similarities slightly above the threshold $S > 0.998$. In the residual image Fig. 6(c) the remaining triples are barely distinguishable from the speckled background intensities. Since the deviation of these skewed triplets from self-similarity depends on their 3d position, a matching algorithm that uses equilateral triplet templates of variable size [34] was not used here.

4.1. Determining the wall position

To find the exact wall position y_0 for the determination of $\vec{\tau}_w$, the 3d position of particles stuck to the wall was determined. An example of these "sticky particles" is provided in Fig. 3(c). The wall shift was determined from the particle positions on the wall (x, y_0, z) using a linear fit $y_0 = mx + nz + o$. The result is shown in Fig. 7. The mean absolute residuals of the plane fit are $3\,\mu m$ to $4\,\mu m$ with a maximum absolute residual of $11\,\mu m$. It can be observed that with increasing speed in the wind tunnel from $u_\infty = 10\,m/s$, the wall position is closer to the reference position, presumably due to a decrease in static pressure in the test section. For the series $u_\infty < 20\,m/s$, average images of each recording were used to determine the wall position. At the highest velocity of $u_\infty = 20\,m/s$, vibrations of the wall in the order of $\pm 2\,\mu m$ were observed (see Fig. 8a) and were accounted for in the calculation of the wall shear stress by applying a sliding minimum over 20 particles images. Deviations from the mean wall shift were additionally low-pass filtered with a cut-off by 200 Hz (see Fig. 8a). The corresponding pre-multiplied power spectral density (PSD) of the wall vibrations shows distinct peaks of structural vibration near 90 Hz (see Fig. 8b).

4.2. Track reconstruction

Using the reconstructed particle positions, Lagrangian particle tracks were initialized with up to four image frames using classical techniques as described by Malik et al. [37] and Ouellette et al. [38]. Starting from the first image, the nearest neighbors in the following image are searched in a domain constrained by a given range of the wall distance variation (10% of Δy), which is considered an appropriate criterion for a wall-bounded flow.

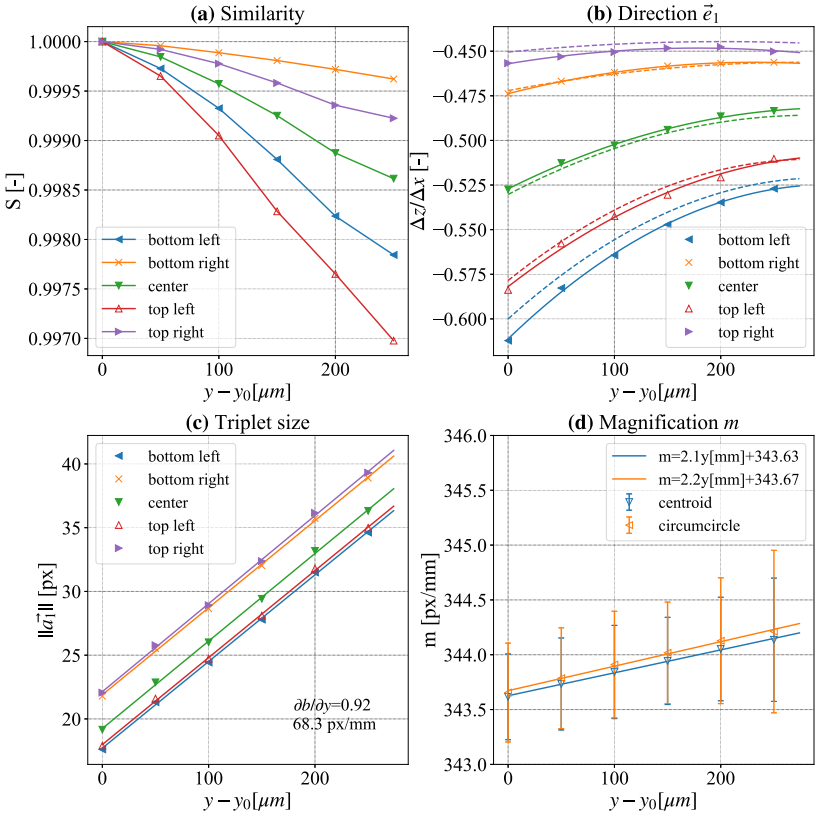

Fig. 5. Geometric calibration parameters for various image regions: (a) Similarity with respect to the nearest wall-position of the calibration plate (b) direction of the triangle side $\vec{e}_1$ including 2nd order polynomial fit (c) calibration curve for $\vec{a}_1$ (d) magnification; y_0 corresponds to the wall position.

Initialization of the predictors towards the second frame on the basis of neighboring tracks in the first frame (cf. 37) was discarded here because, due to high shear rates, only neighbors with approximately equal wall distance and only within a search radius of the Kolmogorov length scale can be considered, which rarely occur at the present low particle image density. On the other hand, the same particle may occasionally disappear and then reappear in the following frame due to varying image intensity or speckle noise. Therefore, the third frame is also included in the nearest neighbor search if no candidate is found in the second frame. Using the displacements between possible particle matches as predictors, candidates are targeted in the third frame within a constant maximum search radius. In the present case, the maximum search radius was set to a constant value $r_{\max} = u'_{\max}\,\Delta t/m$, where $u'_{\max}$ was estimated according to the near-wall maximum of the streamwise velocity fluctuation u' in a ZPG TBL ($u'_{max} \approx \sqrt{8}u_\tau$). If no suitable candidate is found, the fourth frame is also included using twice the previous displacements. From candidates that are linked in three frames, the track with smallest change in velocity is selected (e.g. minimum acceleration criterion). To continue tracks beyond three members, the predicted displacement towards following frames is based on the velocity difference to the predecessor plus the displacement extrapolated from the acceleration in the previous two frames. For longer tracks, the predictor relies on a cubic b-spline fitted through the last four track members. After forward tracking is performed over a set of frames, shortest tracks that consist of less then 4–5 members are removed. With the spurious tracks removed, the entire tracking procedure is repeated for the remaining non-linked particles in backward time association, followed by removal of short tracks.

To obtain the particle position and velocity from the reconstructed track, least-squares regression is applied using a cubic b-spline fitting scheme. Weighting is applied at each vertex, using the absolute disparity δy plus a relaxation offset so that the weight becomes $(\delta y + 2\,\mu\text{m})^{-1}$.

A compilation of 0.2 % of the tracks recorded at $u_\infty = 5.2\,\text{m/s}$ is shown in Fig. 9(a) and demonstrates multiple tracks within the viscous sublayer and a clear spatial variation in velocity within the sublayer with a sharp drop in flow velocity as the wall is approached. In addition, Fig. 9(b) demonstrates the occurrence of linear high speed and meandering low speed tracks also observed in earlier experiments in TBL flows (see e.g. 21,39). The supplementary animation of tracks (see Appendix D) illustrates this and occasionally also sudden changes in direction in the sublayer across the span.

4.3. Uncertainty estimation

For tracer-based measurements, the WSS is estimated by the velocity gradient in the vicinity of the wall (cf. Eq. (1)). The two primary sources of uncertainty are the velocity error δu and the error in detecting the wall distance δy. The relative error ϵ_τ of the WSS can then be estimated using the classical laws of error propagation:

$$\epsilon_{\tau_w}(y) = \frac{\delta\tau_w}{\tau_w} = \left[{\epsilon_u}^2 + {\epsilon_y}^2\right]^{0.5} \tag{3}$$

$$= \left[\left(\frac{\delta u(y)}{u(y)}\right)^2 + \left(\frac{\delta y}{y}\right)^2\right]^{0.5} \tag{4}$$

As shown in Fig. 10, each of the relative errors exhibit a steep increase in measurement uncertainty towards the wall. Here, the velocity error $\epsilon_u(y)$ (cf. Fig. 10a) is estimated from the rms of the wall-normal velocity component at the wall, which should ideally be zero and corresponds to the upper limit of uncertainty, whereas the stream- and

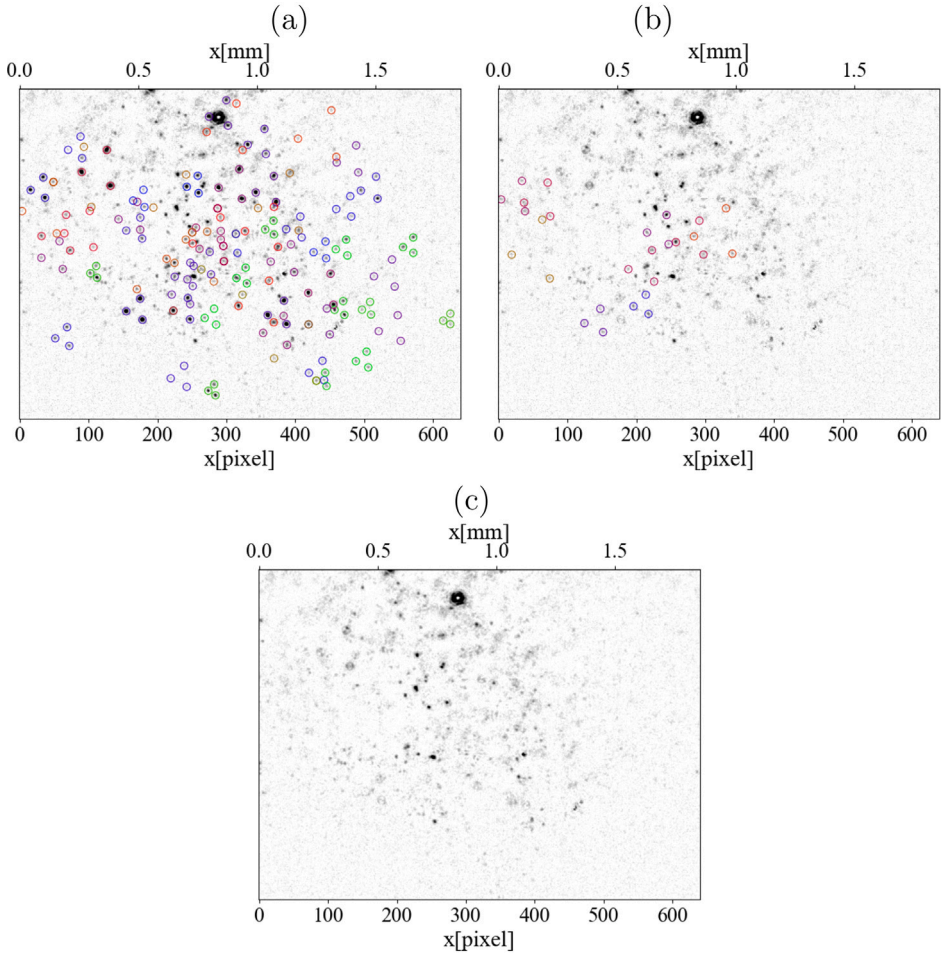

Fig. 6. (a) Processed MA-μPTV sample image from Fig. 3(a) particles that match a triplet are marked by circles of the same color, with the wall distance color-coded (b) second iteration on the residual image (c) residual image with fitted intensities subtracted.

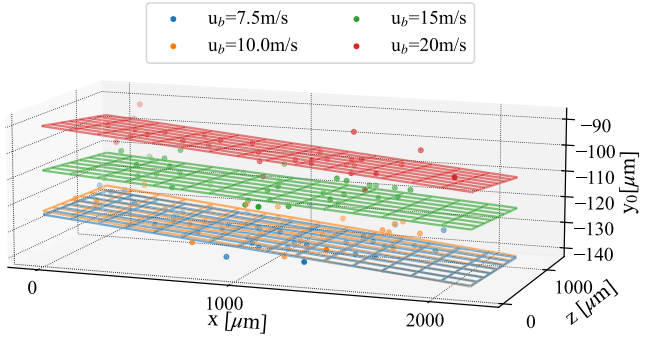

Fig. 7. Plane fit of the wall position obtained from particles stuck to the wall.

spanwise component of particle position should be more accurate due to the higher in-plane resolution. The rms of the wall-normal velocity at y_{min} varied between $[0.02-0.1]$ m/s for the investigated bulk velocity range. If the uncertainty in velocity is instead evaluated from the residuals of the track fitting scheme, i.e. by subtracting the tracked particle positions from their fitted positions, the relative error of the stream- and spanwise velocity components are smaller by a factor of 2 to 4 at the lower bound of the region of interest ($y^+ = 0.6$) (cf. inset axes in Fig. 10a). However, it should be noted that the residual depends on proper weighting of the input of the cubic spline fit (see previous section), which implies that a residual close to zero does not necessarily indicate low noise in the particle positions.

The position error is estimated from the mean absolute disparity of particle reconstruction which is a maximum of ±2.5 μm. When normalized with wall distance, the relative uncertainty $\epsilon_y(y)$ varies between [3–10]% at $y^+ = 0.6$ (cf. Fig. 10b). When plotting the wall distance in micrometer (see inset) the curves collapse with slightly different values at the nearest wall position between [7.5–10]%, which indicates that the position error is less dependent on bulk velocity.

For individual samples, the resulting relative errors of the WSS, indicated by the solid lines in Fig. 10(c), are between [3–20]% in the relevant range of $0.6 < y^+ \leq 4$. Following [40], the 95%-confidence intervals for statistics of mean and the rms can be estimated from single sample uncertainty by

$$\epsilon_{\langle x \rangle} = \frac{1.96}{\langle x \rangle} \sqrt{\frac{\delta_x^2}{N_{s,eff}}} \tag{5}$$

$$\epsilon_{x_{\mathrm{rms}}} = \frac{1.96}{\langle xx \rangle^{0.5}} \sqrt{\frac{\delta_x^2}{2N_{s,eff}}} \tag{6}$$

where $N_{s,eff} < N_s$ is the estimated number of uncorrelated samples within the set N_s and can be obtained by considering the integral time scale for the near-wall flow. Quadrio and Luchini [41] estimated the integral time scale T_u in the viscous sublayer between 19.1 t^* and 19.2 t^*, for which the viscous time unit is defined as $t^* = t_\eta = \nu u_\tau^{-2}$. This time-span covers 20 to 138 laser pulses for the current range of bulk

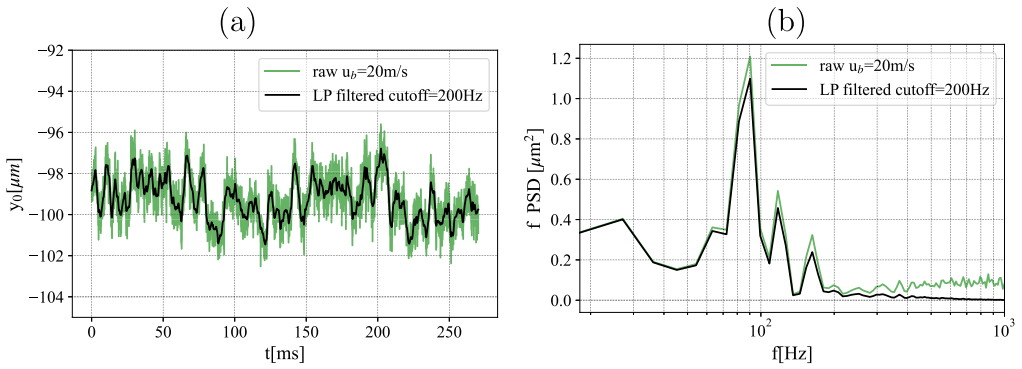

Fig. 8. (a) Wall vibration near image center, (b) pre-multiplied power spectrum of wall vibrations by evaluation of sliding minimum images at $u_\infty = 20\,\mathrm{m/s}$.

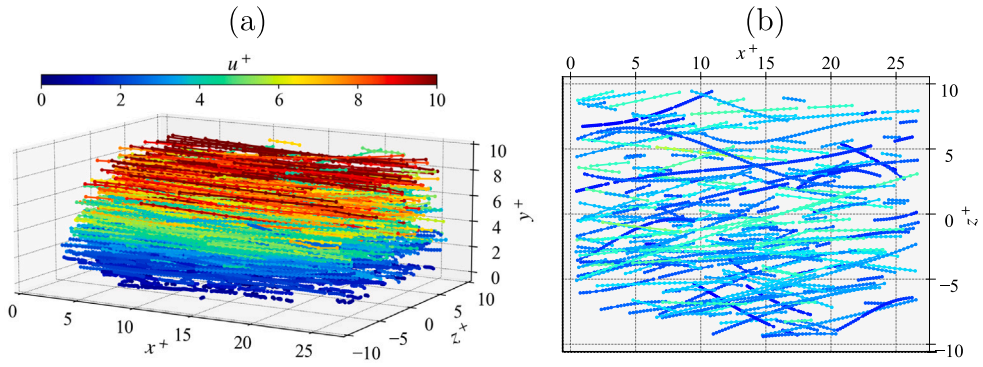

Fig. 9. (a) An accumulation of 0.2% (2000) of the total number of tracks at $u_\infty = 5.2\,\mathrm{m/s}$, $\mathrm{Re}_\tau = 563$, $l^* = 69\,\mu\mathrm{m}$, extracted from 1680 images captured at $f_s = 28\,000$ Hz (b) spanwise meandering tracks in $2 < y^+ < 3$ (x-z projection).

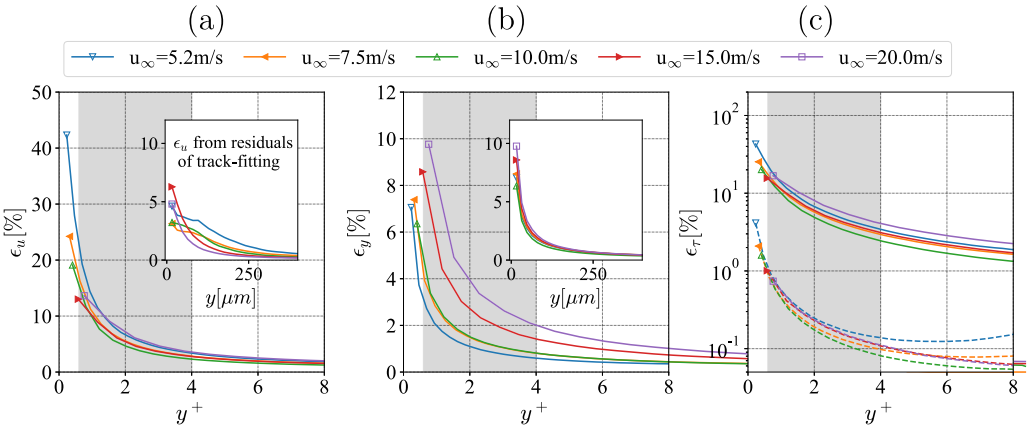

Fig. 10. Relative error estimates for single samples (a) error of normalized velocity based on the variance of the wall-normal velocity at the wall, the inset shows the error based on the streamwise residuum of the track-fitting scheme (b) error of the wall-normal position based on the disparity of particle reconstruction (c) relative error of the WSS, solid lines: single sample, dashed lines correspond to 95% confidence based on Eq. (5); the shaded region correspond to the domain of interest for WSS evaluations.

velocities and sample frequencies between 20 to 37 kHz such that the number of uncorrelated samples can be estimated as follows:

$$N_{s,eff} = \frac{1}{T_u f_s} N_s \approx \frac{u_\tau^2}{19.2\,\nu\, f_s} N_s. \tag{7}$$

When evaluating the limits for 95% confidence for the mean WSS, the dashed lines in Fig. 10(c) indicate a rapid decrease of the random uncertainty by indicating relative errors on the order of [0.1–1]% in the relevant domain of interest of $0.6 < y^+ \leq 4$ (cf. Fig. 10c).

Furthermore, a source of systematic biases is related to the estimation of WSS statistics from finite wall-normal distances within the viscous sublayer [36,42,43]. In particular, when estimating the WSS from mean axial velocity using Eq. (1) linearity within 2% deviation can be assumed for wall distances $y^+ \leq 4$ according to an approximation provided in [42]. Also it is known from DNS that the stream- and spanwise fluctuating WSS vary differently when approaching the wall, which will be the subject of the following discussion of the WSS statistics evaluated in different regions of the viscous sublayer.

5. Results and discussion

5.1. Mean axial velocity and parameter estimation for viscous scaling

To allow comparison with velocity statistics obtained with high-speed profile PIV and numerical data, a bin-averaging scheme with bin heights of $8\,\mu\mathrm{m}$ ($< 0.5\,l^*_{min}$) in wall normal direction was used.

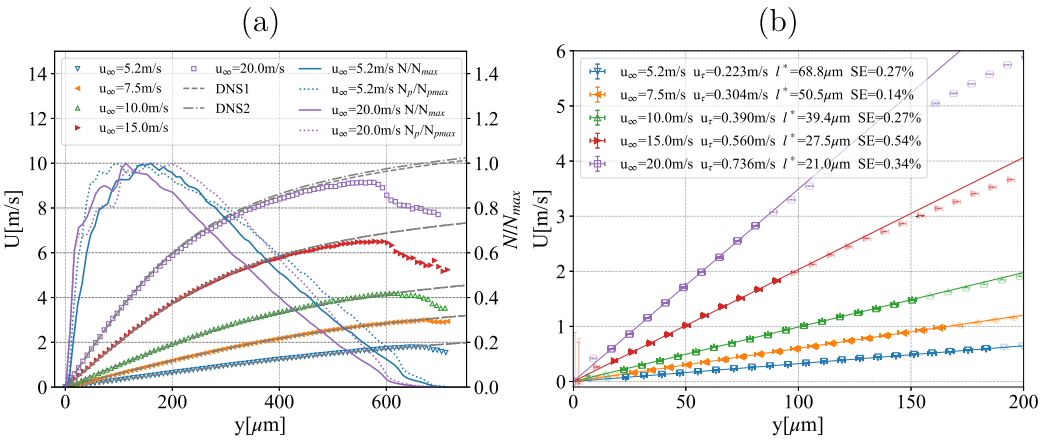

Fig. 11. Mean streamwise velocities from bin averaging of MA-μPTV data (bin height 8 μm): (a) Supplemented by bin counts at the minimum and maximum bulk velocity and profiles form numerical simulations DNS1 [44] and DNS2 [45,46] (b) mean near-wall velocity and linear fit to obtain the wall gradient in $0 < y^+ \leq 4$; error bars indicate the mean absolute disparity and the velocity error using Eq. (5); fading symbols are excluded from the fit.

The assignment into equally spaced bins is performed using bilinear weighting.

In Fig. 11(a), the profiles of the mean axial velocity determined in this way are compared with profiles from DNS/LES and supplemented by the bin counts. In addition, the number of particles N_p (e.g. number of tracks) detected over the wall distance is represented by the dotted lines. While a steep increase in particle counts up to the maximum can be seen on wall-bounded side, they decrease continuously from a wall distance of [100–150] μm up to a distance of [650–700] μm, with the bin counts decreasing almost linearly. Near the wall, the differences in the number of particles between the lowest and highest bulk velocities could be related to the inertia of the particles, with the number of particles being lower at high velocities. Towards the upper edge of the measurement volume, the decrease in particle counts is most likely due to the restricted depth of focus of the method, in which the image intensity decreases at a greater distance from the focus, resulting in a reduced detection rate. In addition, an earlier decrease of bin counts at the higher bulk velocity is due to the camera limitations as the camera framing rate could not be proportionally increased. Therefore, at lower bulk velocities ($u_\infty < 10$ m/s), the mean velocities agree well up to wall distances of 650 μm ($[9.4 - 13]\, l^*$) despite very limited bin counts. For the reasons mentioned, the mean velocity is increasingly underestimated with increasing velocity and wall distance from about $y > 600$ μm ($y^+ > 15$) at $u_\infty = 10$ m/s, from $y > 350$ μm ($y^+ > 13$) at $u_\infty = 15$ m/s and from $y > 170$ μm ($y^+ > 8$) at $u_\infty = 20$ m/s with respect to profiles from DNS. However, it may still be possible to increase the track length further from the wall by reducing the magnification m while maintaining the same frame rate, but at the expense of the accuracy of near-wall velocities and a decreased depth sensitivity.

Fig. 11(b) provides the mean values of the near wall streamwise velocity as obtained from bin averaging of particle tracks. The mean WSS is evaluated by a linear least squares fit of the mean velocity profile. To ensure values inside the linear range only wall distances up to $y^+ < 4$ were considered (faded symbols indicate excluded data points). The error bars represent the mean absolute disparity of the depth reconstruction which is on the order of [1–2.5] μm while the uncertainty in velocity is estimated from the wall-normal variance $\langle vv \rangle$ at the wall and Eq. (5). The gradient fit standard error (SE) on the linear least square fit [47], is between [0.14–0.54] %. Friction velocities and viscous units obtained by this method are provided in Table 2.

5.2. Wall shear stress fluctuations

Fig. 12 provide the stream- and spanwise PDF of the WSS components τ_x' and τ_z' evaluated in the viscous sublayer ($y^+_{min} < y^+ \leq 4$). Per condition the total sample counts range from $[0.28–6.2] \times 10^6$. To collapse the data for different Reynolds numbers, the unsteady WSS estimates are normalized by subtracting the mean and dividing by the root mean square (rms). Some Reynolds number dependency is apparent at the tails of τ_x' which indicates a higher probability of extreme events and confirms similar observations in numerical studies [2,48]. Neglecting reverse flow, a truncated lognormal PDF is fitted within $\tau_x/\tau_{x,\mathrm{rms}} \in [0, 7]$ (see Fig. 12a) and corresponding statistical moments are determined using algebraic expressions. As similarly shown for DNS in Alfredsson et al. [42], the skewness is significantly higher (≈ 10%) due to the one-sided boundedness of the lognormal distribution (see Table 2). The flatness value of the lognormal PDF also exhibit a higher peakness compared to values obtained directly from the distribution without truncation.

The spanwise PDF (see Fig. 12b) qualitatively indicates deviation from a Gaussian distribution with higher probability in the distribution tails also indicated by values above 3 for the flatness, indicating that extreme shear stress events have higher probability compared to a Gaussian distribution. Overall, the distributions agree well with DNS (e.g. Fig. 4b and Fig. 5b in 2), with those obtained with event-based PTV at $\mathrm{Re}_\tau = 563, 754$ (see 36) and with distributions from micro-pillar measurements in a turbulent channel flow (e.g. Fig. 7c and 7d

Table 2
Measured parameters of the wall shear stress obtained from particle velocities in the viscous sublayer in the range $y^+_{min} < y^+ \leq 4$ or extrapolated at the wall ($y^+ = 0$). Moments obtained from a fitted lognormal PDF imply the truncation $\tau_x/\tau_{x,\mathrm{rms}} \in [0, 7]$.

u_∞ [m/s]	5.2	7.5	10.0	15.0	20.0
Symbol	▽	◀	△	▶	□
y^+_{min}	0.01	0.02	0.025	0.15	0.3
u_τ [m/s]	0.223	0.304	0.390	0.560	0.736
l^* [μm]	68.8	50.5	39.4	27.5	21.0
Re_τ	563	754	934	1251	1630
N	6.23×10^6	4.67×10^6	1.78×10^6	4.27×10^5	2.79×10^5
N_{eff}	4.51×10^4	5.22×10^4	1.22×10^4	1.39×10^4	1.37×10^4
$\frac{\tau_{x,\mathrm{rms}}}{\langle \tau_x \rangle}$	0.405	0.422	0.426	0.432	0.438
$\frac{\tau_{x,\mathrm{rms}}}{\langle \tau_x \rangle}$ (lognorm)	0.406	0.422	0.427	0.432	0.437
$\frac{\tau_{x,\mathrm{rms}}}{\langle \tau_x \rangle}$ ($y^+ = 0$)	0.414	–	–	–	–
$\frac{\tau_{z,\mathrm{rms}}}{\langle \tau_x \rangle}$	0.218	0.219	0.224	0.227	0.232
$\frac{\tau_{z,\mathrm{rms}}}{\langle \tau_x \rangle}$ ($y^+ = 0$)	0.286	0.289	0.298	0.299	0.302
S_{τ_x}	0.97	1.04	1.04	1.09	1.11
S_{τ_x} (lognorm)	1.10	1.15	1.19	1.21	1.21
S_{τ_x} ($y^+ = 0$)	0.991	1.02	1.06	1.12	–
S_{τ_z}	0.02	0.02	0.07	0.06	0.03
F_{τ_x}	4.34	4.56	4.52	4.87	4.86
F_{τ_x} (lognorm)	5.22	5.45	5.60	5.69	5.70
F_{τ_x} ($y^+ = 0$)	4.49	4.82	4.76	5.42	5.88
F_{τ_z}	5.69	5.90	5.88	6.20	6.44
F_{τ_z} ($y^+ = 0$)	6.70	7.24	7.46	8.89	9.76

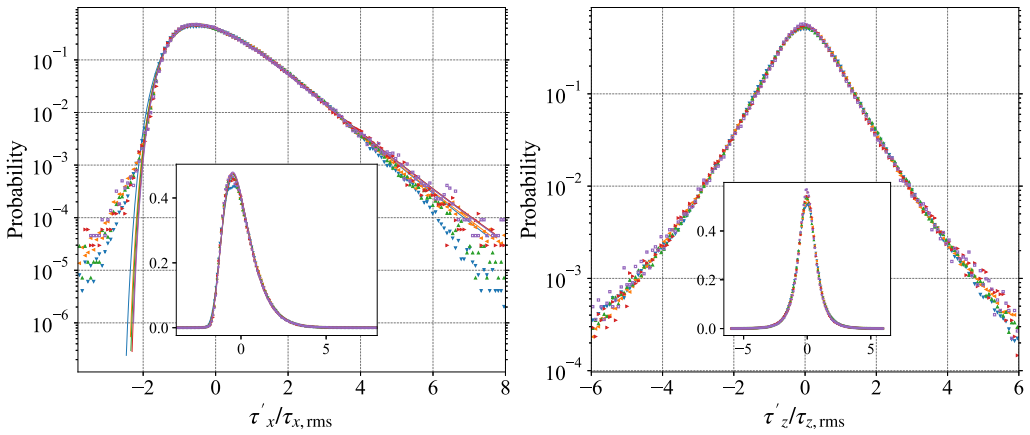

Fig. 12. Streamwise (a) and spanwise (b) distributions of the wall shear rate as determined with MA-μPTV. Lines correspond to a truncated lognormal PDF fitted with $\tau_x/\tau_{x,\mathrm{rms}} \in [0,7]$ and shifted by $-\langle\tau_x\rangle/\tau_{x,\mathrm{rms}}$.

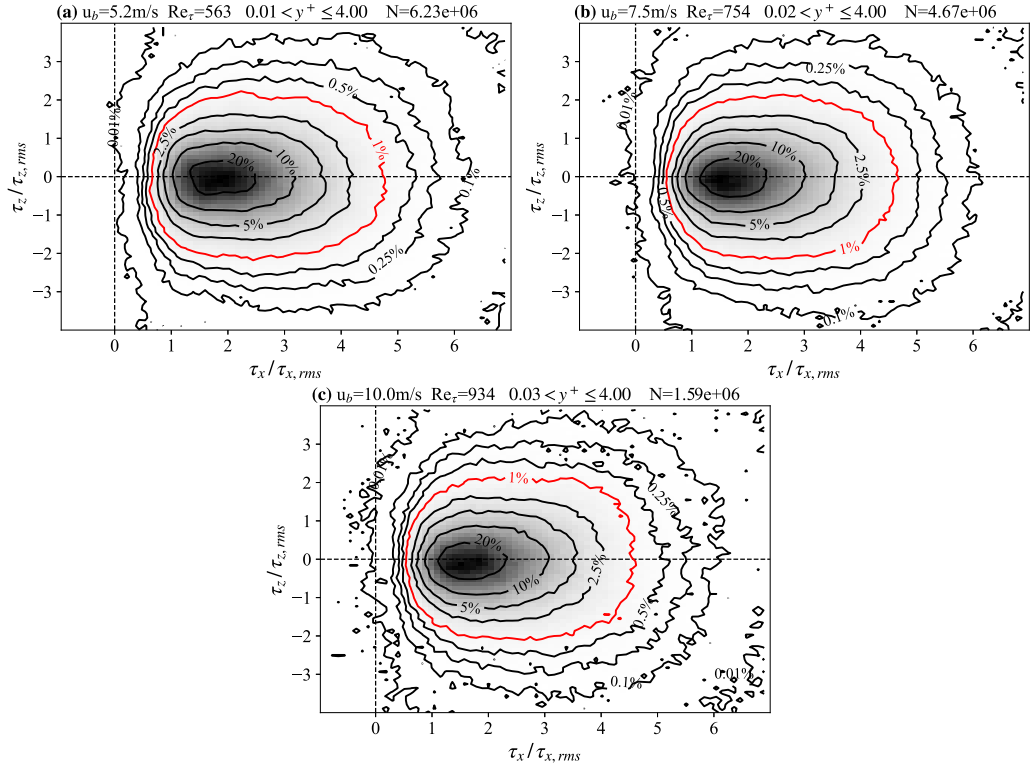

Fig. 13. Joint probability distributions of the stream- and spanwise fluctuations of the WSS (a) $u_\infty = 5.2$m/s (b) $u_\infty = 7.5$ m/s (c) $u_\infty = 10$ m/s.

in 10). With respect to the latter, a better collapse of the distributions at different Reynolds numbers is observed in the present data, and the probability of low stress events in the streamwise direction at $\tau'_x/\tau_{x,\mathrm{rms}} = -2$ is almost an order of magnitude lower.

Fig. 13 shows the corresponding joint probability of stream- and spanwise fluctuations of the WSS vector for different bulk velocities. In order to suppress the distortion of the rms by particles interacting with the wall, the interval for joint probability estimations starts at a wall distance of y_{min}. Reverse flow events appear to occur with an extremely low probability on the order of 10^{-4}. The results indicate similarities with the joint probability distribution measured by Sheng et al. [20] for a turbulent channel water flow at a friction Reynolds number of $\mathrm{Re}_\tau = 1400$ and agree with those obtained with event-based PTV at $\mathrm{Re}_\tau = 563$ (see 36).

We will now focus on the root mean square (rms) of the WSS that can be derived from the near wall particle tracks by extrapolation to the wall. Fig. 14 shows the corresponding profiles of the fluctuating WSS, which were determined from Eq. (1) using a bin averaging scheme with bin heights of 16 μm and bilinear weighting. Because of near-wall deviations between DNS and experiment with regard to velocity fluctuations when normalized by the mean streamwise velocity (see Appendix A), from $u_\infty > 5.2\,\mathrm{m\,s^{-1}}$ the extrapolation of the limits of $\tau_{x,\mathrm{rms}}$ towards the wall is not provided in Table 2. For the remaining datasets, extrapolation is based on a weighted second order polynomial fitting-scheme and the resulting rms values at $y^+ = 0$ are provided in Table 2. Weighting is based on the uncertainty evaluated from Eq. (6).

Current literature provides correlations for the Reynolds number dependency of the rms of WSS components of the form

$$\frac{\tau_{i,\mathrm{rms}}}{\langle\tau_x\rangle} = C_i + 0.018\,ln(\mathrm{Re}_\tau) \tag{8}$$

for which $C_x = 0.298$ is proposed by Örlü and Schlatter [50] for the streamwise fluctuations of the WSS based on previous computational

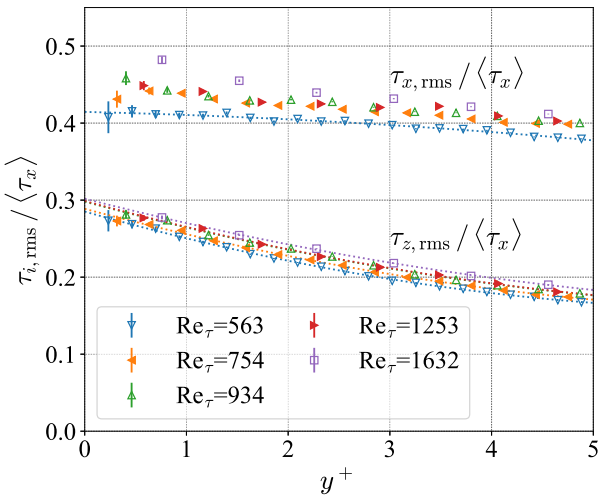

Fig. 14. Near wall fluctuations of the WSS estimates from near-wall tracks. The dotted lines correspond to the weighted 2nd order polynomial fit for estimating the values at the wall.

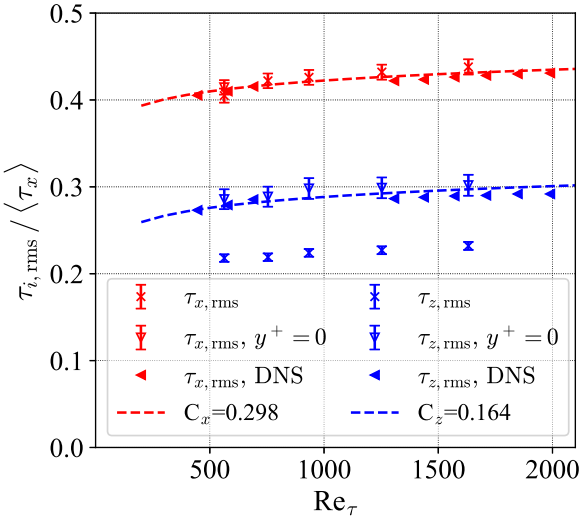

Fig. 15. Root mean squared fluctuations of WSS components determined from particle tracks in the viscous sublayer in $y^+_{min} < y^+ \leq 4$ (×, ×) and extrapolated at the wall (▾, ▾) with uncertainty bound of ±2% and of ±4% for extrapolated values; DNS: [49], dashed lines correspond to Eq. (8) with different offsets $C_x = 0.298$ [50] and $C_z = 0.164$ [2].

and experimental results. For the spanwise fluctuation $\tau_{z,\mathrm{rms}}$ [2] proposed the same logarithmic dependence and a value of $C_z = 0.164$ based on DNS in the range $409 \leq \mathrm{Re}_\tau \leq 720$. Fig. 15 indicates good agreement with the streamwise correlation when comparing rms values obtained from the PDF in Fig. 12(a) and extrapolated values at $u_\infty = 5.2\,\mathrm{m/s}$ (see Fig. 14). With increasing velocity there is a slight systematic overestimation with respect to DNS within a margin of 1.7%, which is probably related to the overestimation of rms values of the normalized fluctuating velocity in the viscous sublayer also visible in Fig. A.1.

Although the same logarithmic dependence is confirmed, values of $\tau_{z,\mathrm{rms}}$ evaluated from the PDF in Fig. 12(b) suggest a significantly lower offset C_z than the correlation by Diaz-Daniel et al. [2] (see Fig. 15). These values are obtained within a wall distance of $y^+_{min} < y^+ \leq 4$, in which the spanwise fluctuations w_{rms}/U decreases rapidly according to the DNS (see Fig. 14 and Fig. A.1). Extrapolation of the values towards the wall using second order polynomials closely match with the correlation with a maximum deviation of 3.8%.

To evaluate the higher order statistics of the WSS (i.e. skewness and flatness factors) and their variations with wall distance, PDFs of the WSS estimates were calculated at various wall-positions for a sample range of $1.8\,l^*$ using Eq. (1). The increase in bin height represents a compromise between a sufficient number of samples and a reasonable spatial resolution in the viscous sublayer. Specifically, PDFs were evaluated for sample ranges of $y^+_i = \pm 0.9$ at positions y^+_i of $y^+_{min}, 1.5, 2.4, 3.3, 4.2$. Corresponding PDFs for $u_\infty = 7.5\,\mathrm{m/s}$ (see Fig. 16) consistently showing the trend that the probabilities for high and low stress events decreases with increasing wall distance for both, the stream- and spanwise component.

The skewness factors $S_{\tau,x}$ obtained by sampling the velocity at different wall distances (see Fig. 17a) increase while approaching the wall and show similar rates of convergence across the Reynolds number range. A similar behavior was observed by Chen et al. [43] (Fig. 7b) who determined unsteady WSS from near wall velocities using reference data from DNS of a channel flow. For the present data, the error bar corresponds to the 95% confidence interval with the classical standard error (SE) of the skewness, whereby the latter is calculated from the number of effective samples (N_{eff}). The resulting relative uncertainties $\epsilon_{S_{\tau,i}} = \pm 0.96\,SE$ are a maximum of ±6% of the streamwise skewness $S_{\tau,x}$. For the data points provided, the extrapolation towards the wall was conducted using a second order polynomial fit (dotted lines in Fig. 17a), for which weighting is provided by SE.

For the most part, the streamwise skewness (see Fig. 17b) largely agrees with DNS values, even at higher Reynolds numbers, with deviations of about 3% for the PDFs obtained within $y^+_{min} < y^+ \leq 4$. Values from extrapolation at the wall show a similar agreement up to $\mathrm{Re}_\tau < 1253$ for which a higher skewness at the wall is predicted albeit within the uncertainty estimate of ±6%. Regarding DNS references and according to [51], it can be assumed that the probability density distributions of the WSS between a ZPG TBL and a channel flow are identical, which justifies our choice of using DNS of channel flow by Hu et al. [48] and ZPG TBL by Diaz-Daniel et al. [2] for our comparisons.

The flatness factors (i.e. kurtosis) of the streamwise WSS estimates exhibit strong variations depending on the choice of sampling volume. This is also visible in the PDFs in Fig. 16, which suggest an increasing probability of extreme events of high and low shear stresses for sampling volumes closer to the wall. Corresponding flatness estimates in Fig. 18(a) confirm this trend with values exceeding three (i.e. Gaussian distribution), while this increase is more significant for the spanwise component τ_z in comparison to the streamwise component τ_x. The study by Chen et al. [43] on the determination of instantaneous wall shear stress from near-wall velocities shows a similar non-linearity for reference values determined from DNS (Fig. 7 c,f), also with a rapid increase of the spanwise flatness with decreasing wall distance, but with a significantly lower dispersion of the limits at the wall of 9.2 to 10 for a similar range of Reynolds numbers. In Fig. 18(a), the error bar corresponds to the 95% confidence interval based on the classical SE of the flatness, calculated from the number of effective samples (N_{eff}). The resulting relative uncertainties $\epsilon_{F_{\tau,i}} = \pm 0.96\,SE$ are a maximum of ±3%.

The Reynolds number dependency of the flatness factors compared to values from DNS is presented in Fig. 18(b) supplemented by the results obtained from PDFs that sample the entire viscous sublayer (see Fig. 12). Clearly, the latter underestimate the flatness from DNS for the aforementioned reason (i.e. high dependency on the wall distance). On the other hand the extrapolated values at $y^+ = 0$ exhibit a better agreement with the DNS references albeit deviations on the order of 6% for the streamwise component and a significant underestimation of the flatness of the spanwise component of the WSS with respect to values from DNS. The latter likely is related to the high non-linearity of the spanwise flatness when derived from near wall velocities which were evaluated in a relatively large sampling depth interval of $1.8\,l^*$ in combination with a high relative uncertainty of the WSS when tracer velocities were captured at wall distances of $y^+ < 1$ (cf. Fig. 10). Another reason could be the lower number of samples when approaching the wall (see Fig. 11a), which results in a higher impact of outlier when calculating the flatness factors from the probability density function (PDF).

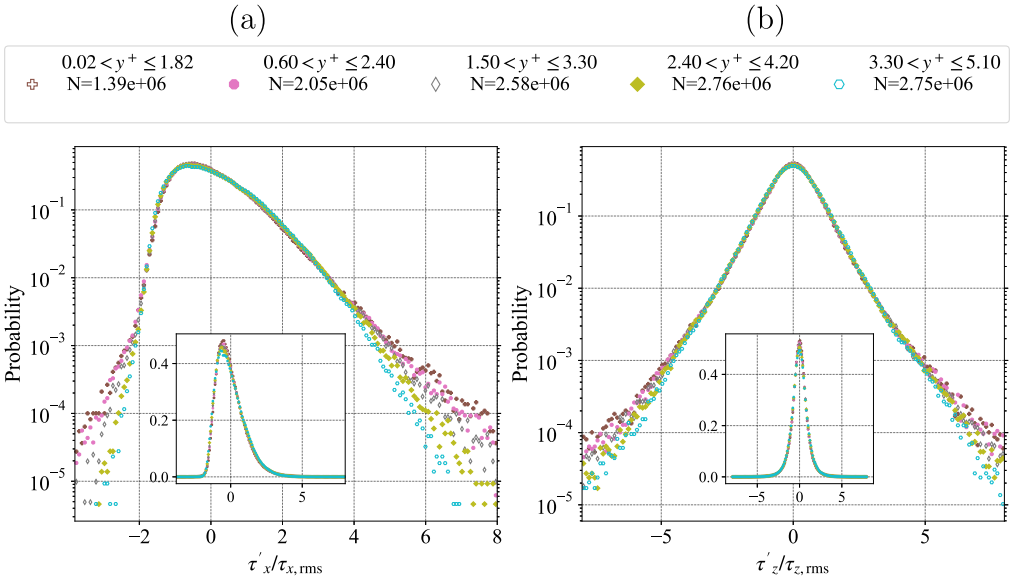

Fig. 16. Streamwise (a) and spanwise (b) distributions of the wall shear rate at different wall-distances for $u_\infty = 7.5$ m/s measured with MA-μPTV.

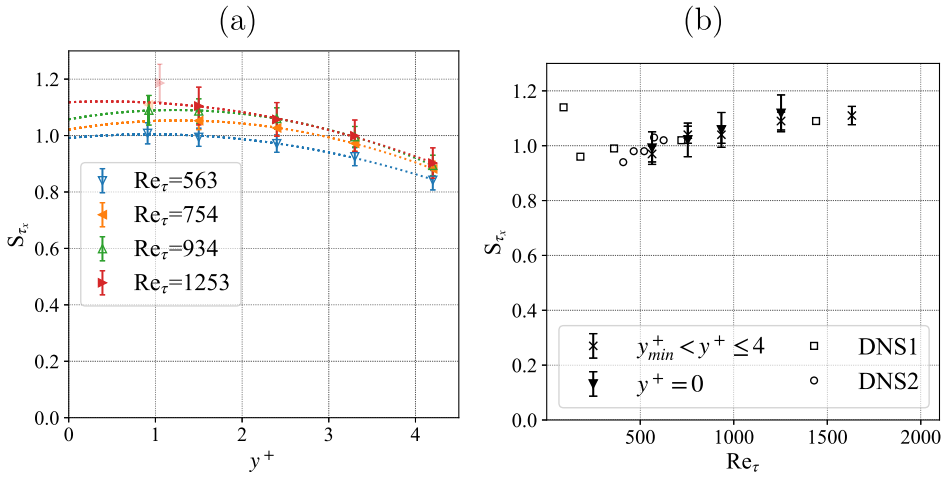

Fig. 17. (a) Skewness factor of the streamwise WSS including standard error evaluated from probability density distributions of sample range $1.8\,l^*$ for $u_\infty = 5.2$, 7.5, 10.0, 15 m/s, The dotted lines correspond to the weighted 2nd order polynomial fit for estimating the values at the wall (b) Reynolds number dependency of skewness with uncertainty bound of ±3% for PDFs evaluated within in $y^+_{min} < y^+ \leq 4$ (×) and extrapolated at the wall (▾) including uncertainty bounds of ±6%; DNS1: [48]; DNS2: [2].

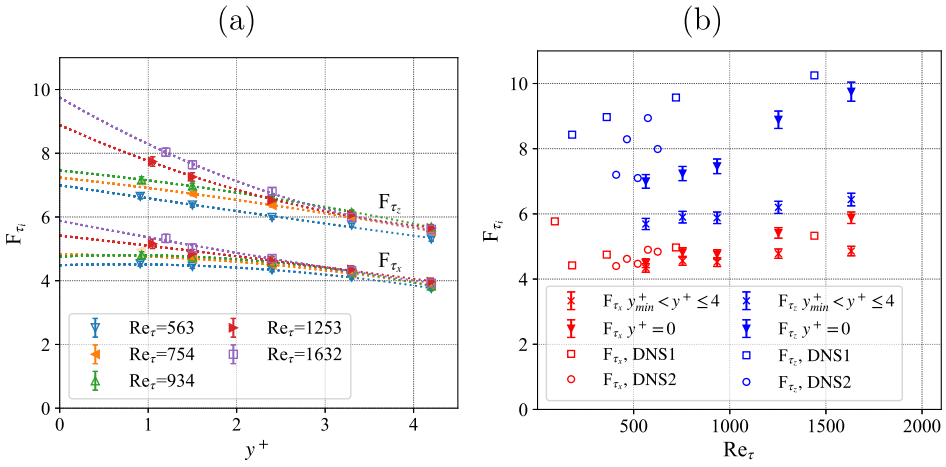

Fig. 18. (a) Flatness values of unsteady WSS evaluated from probability density distributions of sample range $y_i^+ \pm 0.9$ for $u_\infty = 5.2$, 7.5, 10.0, 15, 20 m/s, The dotted lines correspond to the weighted 2nd order polynomial fit for estimating the values at the wall (b) Reynolds number dependency of Flatness with uncertainty bound of ±3% for PDFs evaluated within in $y^+_{min} < y^+ \leq 4$ (×, ×) and extrapolated at the wall (▾, ▾); (normal distribution: $F_{\tau_i} = 3$) DNS1: [48]; DNS2: [2].

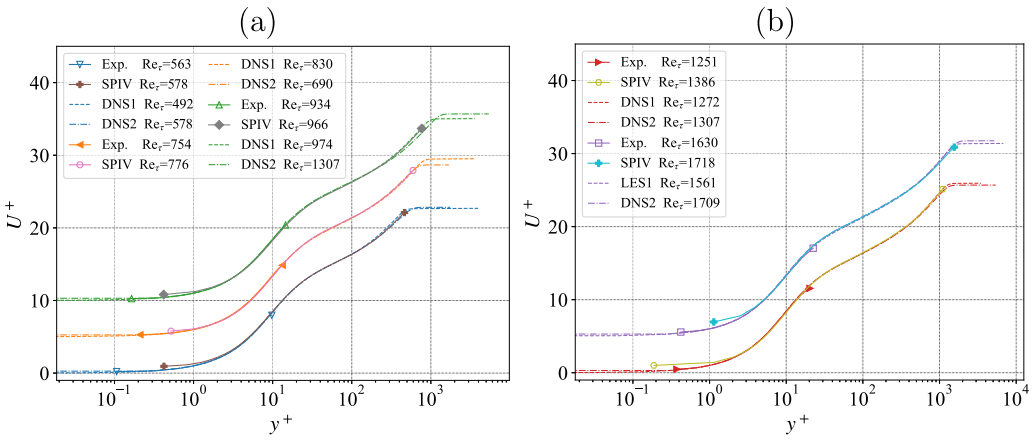

Fig. 19. Mean streamwise velocities at viscous scaling supplemented by profiles from stereoscopic high-speed profile PIV and numerical simulations of a ZPG TBL; DNS1/LES1: [44] and DNS2: [45,46]; velocities are offset by $5u^+$ (a) $u_\infty = 5.2, 7.5, 10.0\,\mathrm{m/s}$ (b) $u_\infty = 15, 20\,\mathrm{m/s}$.

5.3. Velocity statistics and comparison with DNS

In this section, we assess the extent to which the velocity profiles measured with MA-μPTV agree with the profiles from DNS and from reference measurements with stereoscopic high-speed profile PIV (HS-SPIV), even beyond the viscous sublayer.

Mean velocity profiles for all free stream conditions are provided in Fig. 19, normalized by the corresponding viscous unit and friction velocity. Profiles measured with HS-SPIV indicate a clear logarithmic region and the beginning of the wake region as expected for this type of flow. Up to the beginning of the logarithmic region the mean streamwise velocity agrees well with DNS and LES data of a ZPG TBL from two sources [44,46], which is an important 'proof of concept' for an accurate determination of the viscous scaling with MA-μPTV. At the highest Reynolds number, at wall distance greater $y^+ > 8$, the mean velocity obtained from MA-μPTV (legend entry *Exp.*) is slightly underestimated which indicates the loss of faster particle tracks due to limitations of the present high speed camera configuration. This was already discussed in Section 5.1 that depending on friction velocity, an underestimation arises for wall distances of $8 < y^+ \leq 13$.

It can be seen that HS-SPIV and MA-μPTV are complementary techniques that cover different regions of the boundary layer profile with an overlap in the buffer layer. While strong near-wall gradients are a challenge for HS-SPIV, even with narrow window sizes of 48×6 pixels, data within the viscous sublayer ($y^+ \leq 4$) can only be captured reliably using PTV, especially at higher velocities (smaller viscous scales).

Fig. 20 indicates that $\langle u'u' \rangle$ is in good agreement with DNS and LES up to $y^+ = 8$. Beyond this wall distance, limitations in the focal depth of MA-μPTV and the lower proportion of fast tracks result in the reduced convergence of second order statistics and an overestimation of the streamwise variance. With increasing friction velocity the "inner peak" shifts towards the wall, to $y \approx 230\,\mu\mathrm{m}$ at $u_\infty = 20\,\mathrm{m/s}$, and the over-estimation seems to be partially compensated with the increase in bin counts. The peak height, although not converged, is reproduced within the range provided by numerical simulations in Fig. 20(b). Deviations between DNS and HS-SPIV for the spanwise and streamwise variance especially occur at the two highest bulk velocities and are most likely due to spatial filtering of small structures by the finite sized interrogation window used for PIV.

Both MA-μPTV and HS-SPIV match the profiles of the wall-normal $\langle v'v' \rangle$ variances predicted by DNS/LES approximately up to $y^+ \leq 10$. The same is valid for the spanwise variance $\langle w'w' \rangle$, with a systematic overestimation within the viscous sublayer and buffer layer for HS-SPIV, which increases with increasing tunnel speed. In contrast, at higher velocities $u_\infty = 15, 20\,\mathrm{m/s}$ from $y^+ > 6$ (see Fig. 20b), there is a systematic underestimation of the DNS reference of the spanwise variance in the MA-μPTV measurements, probably because in the buffer layer the fastest spanwise meandering particle tracks are underrepresented due to limitations in the camera frame rate.

In general, for MA-μPTV the spanwise variance in the viscous sublayer ($y^+ < 4$) matches DNS with minor underestimation. For HS-SPIV the over-prediction of the spanwise component could be explained by the low opening angle between the cameras of about 25° (cf. Appendix C, Fig. C.1) which is associated with a three times larger uncertainty of the spanwise component in comparison to the streamwise component.

Remarkably, Fig. 21 indicates, that for the lowest Re_τ, profiles from MA-μPTV of streamwise velocity skewness S_u and flatness F_u factors coincide very well with values from DNS in the range of measurement $0.2 \leq y^+ \leq 10$, although more data is required to get a smooth curve. For the remainder of the test points, the skewness (cf. Fig. 21a) agrees with DNS in the range $2 \leq y^+ \leq 6$. Deviation from DNS above a wall distance $y^+ > 6$ is probably related to underrepresented fast particle tracks. Also from this wall distance, the under-representation of faster tracks in the buffer layer and the overestimation of the streamwise variance due to increasing noise seem to result in a slight overestimation of the skewness with respect to the DNS. On the other hand, for $\mathrm{Re}_\tau \geq 754$ in the wall distance range $y^+ = [1 - 2]$, the measured flatness F_u (cf. Fig. 21b) agrees very well to values from DNS within the measurement scatter of data points related to a insufficient sample count to achieve a smooth curve.

6. Conclusion & outlook

The present results give a strong indication that multi-aperture microscopic particle tracking velocimetry (MA-μPTV) is a viable non-contact technique for accurate measurements of the unsteady wall shear stress (WSS) vector using only a single access port. The equipment requirements are relatively low compared to setups relying on multiple camera configurations with side-scattering illumination. The technique is validated with measurements of a turbulent boundary layer of zero pressure gradient (ZPG) at shear velocities up to $0.74\,\mathrm{m\,s^{-1}}$ and shear Reynolds numbers up to 1630 using corresponding DNS as reference. Since the relative uncertainties in tracer velocity and wall distance increase significantly in proximity of the wall, the resulting random error of the WSS fluctuations was estimated to be of the order of $[0.1 - 1]\%$ in the relevant range of wall distances given the actual number of effective samples. The depth-of-field beyond which the mean streamwise velocity begins to be underestimated represents the upper spatial limit of the present imaging configuration ($f_{max} = 37\,\mathrm{kHz}$, $m = 4.5$, $d = 2\,\mathrm{mm}$, $D = 8.2\,\mathrm{mm}$). For the present range of friction velocities, these upper limits are in the range of $[250 - 650]\,\mu\mathrm{m}$ in the wall-normal direction and thus far beyond the thickness of the viscous

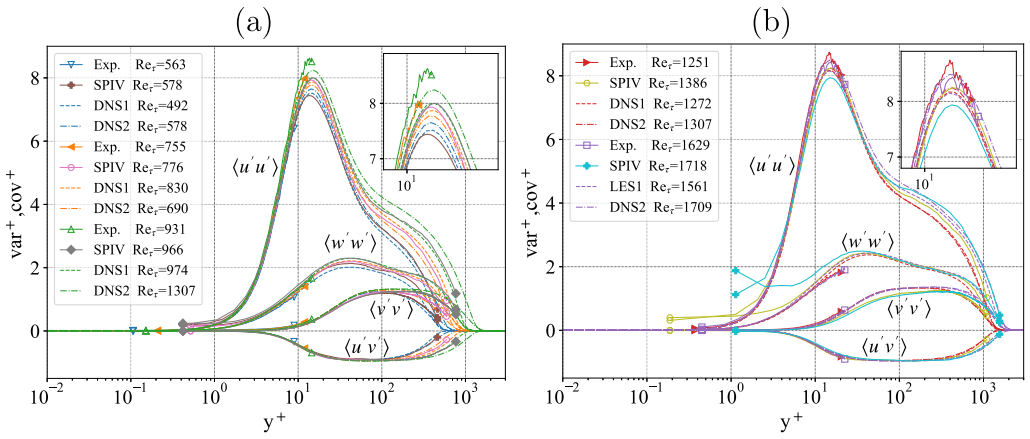

Fig. 20. Fluctuating velocities at viscous scaling supplemented by profiles from HS-SPIV and numerical simulations of a ZPG TBL; DNS1/LES1: [44] and DNS2: [45,46]; (a) u_∞ = 5.2, 7.5, 10.0 m/s (b) u_∞ = 15, 20 m/s.

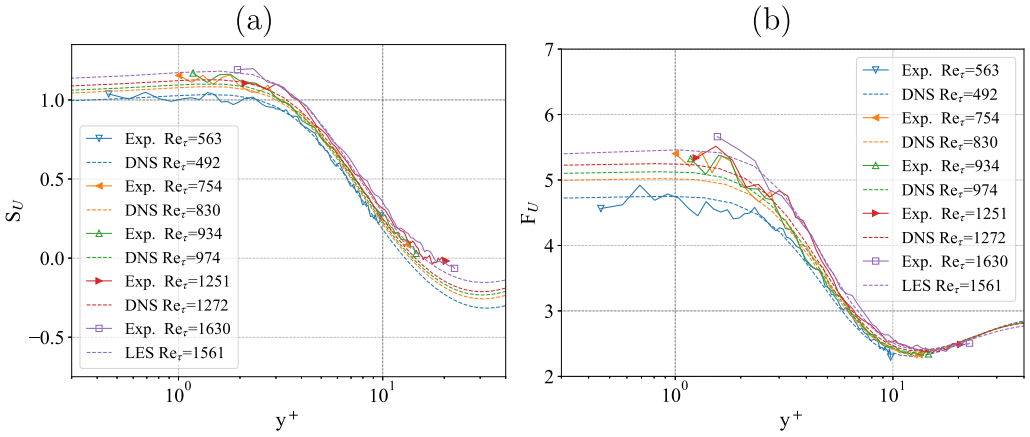

Fig. 21. (a) Skewness S_u and (b) flatness F_u of streamwise velocity supplemented by profiles from numerical simulations of a ZPG TBL by [44].

sublayer. In the viscous sublayer the probability density function (PDF) of both components of the WSS could be reliably captured down to probability densities of 10^{-3}. To the best of our knowledge, this has not been achieved in the past in experiments, particularly not for the spanwise component. For the streamwise component the measured Reynolds number dependency of $\tau_{x,\mathrm{rms}}$ agrees to correlations by [50] with a maximum residuum of 1.7 % for a probability density distribution captured in the in the range to $y_{min} < y^+ \leq 4$. The remaining systematic bias depends on the wall-normal sampling interval for which the corresponding PDF is acquired. It is demonstrated, that underestimation of the fluctuations of the spanwise WSS is related to the rapid nonlinear decrease with the wall-distance for both quantities $u_{z,\mathrm{rms}}/\langle u_x \rangle$ and $\tau_{z,\mathrm{rms}}/\langle \tau_x \rangle$. In effect, it results in a bias on the order of −30% with respect to fluctuations at the wall estimated from a correlation by Diaz-Daniel et al. [2]. To remedy this, the PDFs and rms values are calculated at several points within the viscous sublayer allowing an estimation of the rms values at the wall through extrapolation. With a maximum deviation of 3.8%, the resulting values agree well with the correlation for the spanwise WSS fluctuations. In addition, the skewness factor of the streamwise WSS component, S_{τ_x}, agrees well with values from the literature within the estimated uncertainty of 3 %.

Profiles of velocity statistics are obtained by bin averaging at a spatial resolution of 8 µm ($< 0.5\, l^*_{min}$) or 0.6 pixel. Up to the buffer layer, profiles of the mean streamwise velocity agree well with DNS and LES of a ZPG TBL, which indicates an accurate determination of both: near-wall velocities and viscous scaling. Excellent agreement with DNS data is obtained at similar Reynolds numbers for variances and covariance of the velocity components. Although the number of samples is not sufficient to obtain a smooth profile, skewness and flatness factors agree to values from DNS at similar Reynolds numbers within the random uncertainty especially for the lowest bulk velocity. For the remainder of the test points, the skewness agrees with DNS in the range $2 \leq y^+ \leq 6$ beyond which faster particle tracks are underrepresented.

In conclusion, it can be stated that measurements of the unsteady WSS vector at unprecedented levels of accuracy and resolution have been presented herein. It is important to note, that the applicability of the technique does not depend on the shear Reynolds number of the flow itself, which also depends on BL thickness, but rather on the size of the viscous unit. Using faster cameras this could be further increased to much higher u_τ as resolving viscous scales down to O(10 µm) is feasible with the current lens magnification. As an alternative, high magnification 3D-STB [52] holds similar potential but requires 3–4 high-speed cameras of comparable performance (see e.g. 53). By using modern high-speed cameras with frame rates exceeding 40 kHz along with a 3 to 4 times longer field of view (FOV) in streamwise direction would extend the velocity range and thus the depth of the measurement volume by increasing the yield in longer tracks in the buffer layer. To reduce the problem of low particle image density and thus achieve a higher number of samples per data set, a larger field of view should be captured, e.g. by using microscope optics with lower magnification in combination with cameras with smaller pixels, which in turn requires a proportionally higher laser power to obtain the same signal-to-noise ratio of the triplet particle images.

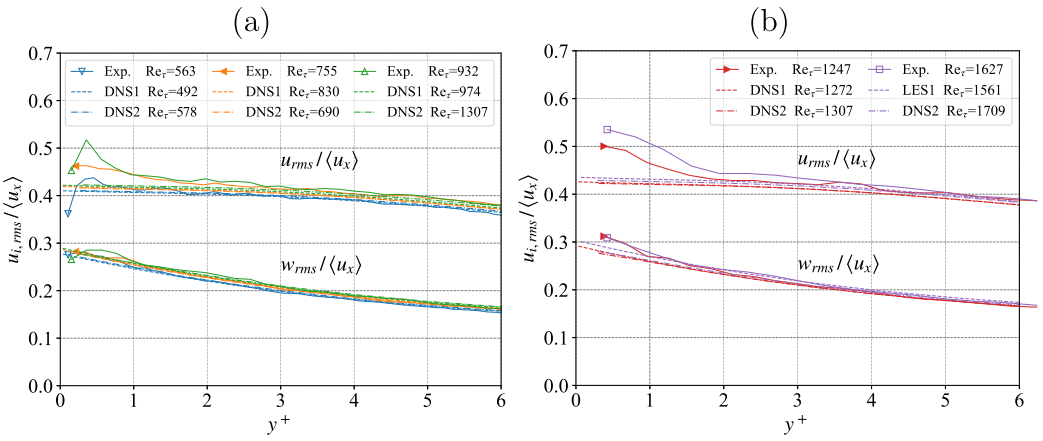

Fig. A.1. Near wall fluctuating velocities divided by the mean streamwise velocity supplemented by profiles from numerical simulations of a ZPG TBL; DNS1/LES1: [44] and DNS2: [45,46]; (a) u_∞ = 5.2, 7.5, 10.0 m/s (b) u_∞ = 15, 20 m/s; the bin height is 8 µm.

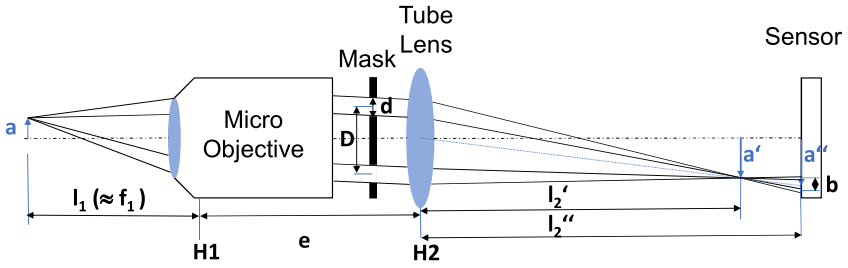

Fig. B.1. Optical configuration for MA-µPTV with infinity-corrected microscope objective and tube lens.

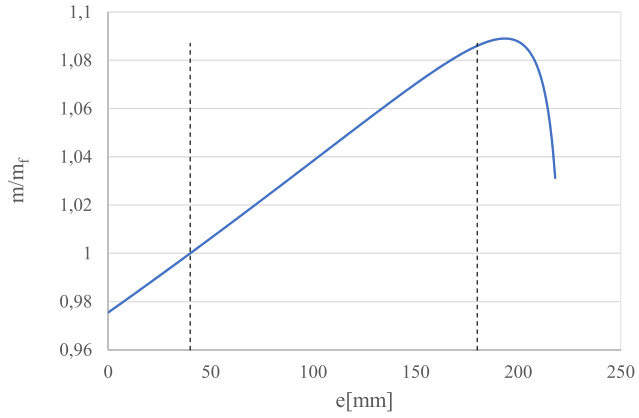

Fig. B.2. Ratio of the image magnification m at the far edge of the volume and the focal magnification m_f near the wall for different distances between the microscope objective and the tube lens.

CRediT authorship contribution statement

Joachim Klinner: Writing – review & editing, Writing – original draft, Visualization, Validation, Software, Methodology, Investigation, Formal analysis, Conceptualization. **Christian E. Willert:** Writing – review & editing, Writing – original draft, Validation, Supervision, Software, Methodology, Investigation, Formal analysis, Conceptualization.

Funding

This work was made possible through DLR-internal funding.

Declaration of competing interest

The authors declare that they have no known competing financial interests or personal relationships that could have appeared to influence the work reported in this paper.

Acknowledgments

We are very grateful for the support by our colleagues of DLR Institute of Aerodynamics and Flow Technology during our measurement campaign in Göttingen, in particular Prof. Markus Raffel and his team for the use of the wind tunnel facility and Prof. Andreas Schröder for providing the high-speed cameras used herein.

Appendix A. Limiting behavior of velocity fluctuations

Following Alfredsson et al. [14] and Li et al. [15] fluctuations of the WSS can as well be estimated from velocity fluctuations when normalized by the mean streamwise velocity using the following relation:

$$\frac{\tau_{i,\mathrm{rms}}}{\langle\tau_x\rangle} \approx \lim_{y\to 0}\frac{u_{i,rms}}{\langle u_x\rangle} \tag{A.1}$$

The limiting behavior of normalized velocity fluctuations is shown in Fig. A.1 for both, experimental and numerical data. The DNS predicts a gradual increase of the streamwise fluctuations from $y^+ < 3$ while the spanwise component increases by approximately 35% when approaching the wall. It can be clearly seen that the spanwise experimental data follow this trend very well up to a wall distance of $y^+ = [1\text{–}2]$. On the other hand, from $u_\infty > 5.2\,\mathrm{m\,s^{-1}}$ the streamwise fluctuations show a slight positive offset from the DNS, which increases significantly from $y^+ < 2$, especially for the two highest velocities (cf. Fig. A.1b). For velocities $u_\infty > 10$m/s, this deviation between experiment and DNS of about 20% cannot be explained by a different

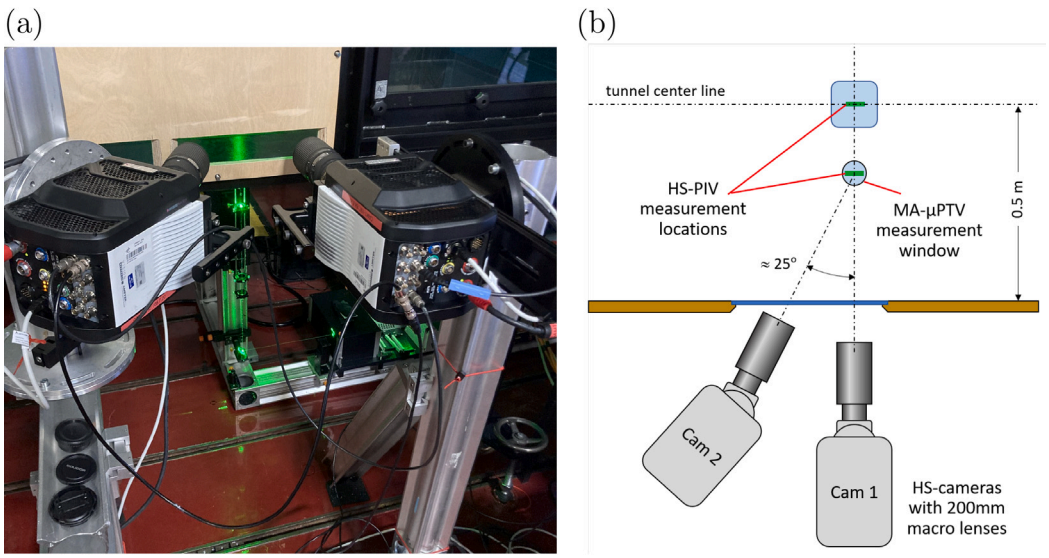

Fig. C.1. Camera setup for stereoscopic high-speed profile PIV measurements.

accuracy for stream- and spanwise velocities as the residuals of the track fitting scheme only differ by 2% in x and z at a wall distance of $y^+ = 1$. Therefore, at the time of writing, there is no plausible explanation of the bias that could be related to the specifics of the experimental imaging setup or statistical uncertainty.

Appendix B. Optical characteristics of the multi-aperture microscopic system

The calibration curve in Fig. 5(d) shows that, in contrast to convex singlets, the magnification increases with increasing object distance. This can be explored in more detail by considering the two-stage defocusing optical configuration used here, as shown in Fig. B.1, where the image position of a particle is a''. The total magnification between object an sensor plane is $m = m_1\, l_2''/l_2'$, with $m_1 = a'/a$. If the particle is at the focal plane, m_1 becomes $m_f = f_2/f_1$ where f_1 and f_2 are the focal length of microscope objective and tube lens. For small changes in the object distance Δl_1, it can be shown, that the image distance $\Delta l_2'$ varies greatly according to $\Delta l_2' = -m_1^2\, \Delta l_1$. In other words: If the distance of particle to the focal plane increases, the image distance l_2' decreases by about 20 times this distance in the present configuration. On the other hand, m_1 decreases only slightly with increasing wall distance, which leads to an increase of m in a specific range of e as can be shown by applying the following relations. The total focal length of a system of two thin lenses is

$$f = \frac{f_1\, f_2}{f_1 + f_2 - e} \tag{B.1}$$

where f_1 and f_2 are the focal length of microscope objective and tube lens and e is the spacing between the principle planes of both lenses [54]. The spacing of the image sided principle planes of the overall system then becomes [54]

$$\overline{H_2 H'} = \frac{f_2\, e}{e - f_1 - f_2} \tag{B.2}$$

In the present MA-μPTV system, e cannot be measured precisely and is estimated with 40 mm to 60 mm, as the actual principal planes, H_1, H_2 of the microscope objective and the tube lens are not specified by the manufacturer. By applying the previous equations for the given range of e in combination with the thin lens equation, it is evident that the total magnification m becomes slightly larger than the focal magnification m_f if $f_1 < e < f_2$ as shown in Fig. B.2.

Appendix C. High-speed profile PIV reference measurements

Comparative measurements of the TBL are provided through high-speed profile PIV [17] which also provides accurate estimates of relevant TBL parameters such as the edge velocity, BL thickness, momentum and displacement thickness along with the corresponding Reynolds numbers in Table 1. For these measurements a FOV of $4.0 \times 51.2\,\mathrm{mm}^2$ (160×2048 pixels) captured the complete boundary layer height and part of the undisturbed flow at camera framing rates of 10 kHz to 40 kHz. For each free stream velocity, $n_r = 8$ records of $n_f = 38\,000$ images were obtained covering between 350 and 550 boundary layer turn-over periods per record.

In a second set of measurements the 2d-2c HS-PIV setup is extended with a second camera to provide stereoscopic 2d-3c data of the flow field thereby allowing for the recovery of the spanwise velocity component w (see Fig. C.1). The viewing angle between the cameras is approximately 25°. Magnification is increased by 50 % to provide a reduced FOV of $2.5 \times 32.5\,\mathrm{mm}^2$ at about $16\,\mu\mathrm{m\,pixel}^{-1}$. At the lowest velocity of $u_\infty = 5.2$ m/s this corresponds to about 4.3 pixel/l^* reducing to 1.3 pixel/l^* at $u_\infty = 20$ m/s. The image data is processed using a triple-frame cross-correlation based algorithm with iterative grid refinement.

When processed with samples of 48×6 pixel, effects due to spatial smoothing arise that in particular attenuate estimates of the velocity variances with increasing velocities [55] and prevent reliable measurements in single viscous unit range.

Appendix D. Supplementary material

Animated sequences of the acquired triplet image data and recovered near-wall particle tracks are provided as supplementary material.

Supplementary material related to this article can be found online at https://doi.org/10.1016/j.expthermflusci.2024.111395.

Data availability

Data will be made available on request.

References

[1] H. Abe, H. Kawamura, H. Choi, Very large-scale structures and their effects on the wall shear-stress fluctuations in a turbulent channel flow up to Re_τ = 640, J. Fluids Eng. 126 (5) (2004) 835–843, http://dx.doi.org/10.1115/1.1789528.

[2] C. Diaz-Daniel, S. Laizet, J.C. Vassilicos, Wall shear stress fluctuations: Mixed scaling and their effects on velocity fluctuations in a turbulent boundary layer, Phys. Fluids 29 (5) (2017) 055102, http://dx.doi.org/10.1063/1.4984002.

[3] J.I. Cardesa, J.P. Monty, J. Soria, M.S. Chong, The structure and dynamics of backflow in turbulent channels, J. Fluid Mech. 880 (2019) R3, http://dx.doi.org/10.1017/jfm.2019.774.

[4] B. Guerrero, M.F. Lambert, R.C. Chin, Extreme wall shear stress events in turbulent pipe flows: spatial characteristics of coherent motions, J. Fluid Mech. 904 (2020) A18, http://dx.doi.org/10.1017/jfm.2020.689.

[5] M. Fischer, J. Jovanović, F. Durst, Reynolds number effects in the near-wall region of turbulent channel flows, Phys. Fluids 13 (6) (2001) 1755–1767, http://dx.doi.org/10.1063/1.1367369.

[6] P.A. Gubian, J. Stoker, J. Medvescek, L. Mydlarski, B.R. Baliga, Evolution of wall shear stress with Reynolds number in fully developed turbulent channel flow experiments, Phys. Rev. Fluids 4 (7) (2019) 074606, http://dx.doi.org/10.1103/PhysRevFluids.4.074606, Publisher: American Physical Society.

[7] A. Perez, R. Örlü, A. Talamelli, P. Schlatter, Appraisal of cavity hot-wire probes for wall-shear-stress measurements, Exp. Fluids 63 (9) (2022) 151, http://dx.doi.org/10.1007/s00348-022-03498-3.

[8] R. Örlü, R. Vinuesa, Instantaneous wall-shear-stress measurements: advances and application to near-wall extreme events, Meas. Sci. Technol. 31 (11) (2020) 112001, http://dx.doi.org/10.1088/1361-6501/aba06f, Publisher: IOP Publishing.

[9] E.P. Gnanamanickam, B. Nottebrock, S. Große, J.P. Sullivan, W. Schröder, Measurement of turbulent wall shear-stress using micro-pillars, Meas. Sci. Technol. 24 (12) (2013) 124002, http://dx.doi.org/10.1088/0957-0233/24/12/124002.

[10] Y. Liu, M. Klaas, W. Schröder, Measurements of the wall-shear stress distribution in turbulent channel flow using the micro-pillar shear stress sensor MPS3, Exp. Therm Fluid Sci. 106 (2019) 171–182, http://dx.doi.org/10.1016/j.expthermflusci.2019.04.022.

[11] Fukang Jiang, Yu-Chong Tai, B. Gupta, R. Goodman, S. Tung, Jin-Biao Huang, Chih-Ming Ho, A surface-micromachined shear stress imager, in: Proceedings of Ninth International Workshop on Micro Electromechanical Systems, IEEE, San Diego, CA, USA, 1996, pp. 110–115, http://dx.doi.org/10.1109/MEMSYS.1996.493838.

[12] M. Kimura, S. Tung, J. Lew, C.M. Ho, F. Jiang, Y.C. Tai, Measurements of wall shear stress of a turbulent boundary layer using a micro-shear-stress imaging chip, Fluid Dyn. Res. 24 (6) (1999) 329–342, http://dx.doi.org/10.1016/S0169-5983(99)00002-7.

[13] J.D. Ruedi, H. Nagib, J. Österlund, P.A. Monkewitz, Unsteady wall-shear measurements in turbulent boundary layers using MEMS, Exp. Fluids 36 (3) (2004) 393–398, http://dx.doi.org/10.1007/s00348-003-0666-1.

[14] P.H. Alfredsson, A.V. Johansson, J.H. Haritonidis, H. Eckelmann, The fluctuating wall-shear stress and the velocity field in the viscous sublayer, Phys. Fluids 31 (5) (1988) 1026–1033, http://dx.doi.org/10.1063/1.866783.

[15] W. Li, D. Roggenkamp, W. Jessen, M. Klaas, W. Schröder, Reynolds number effects on the fluctuating velocity distribution in wall-bounded shear layers, Meas. Sci. Technol. 28 (1) (2017) 015302, http://dx.doi.org/10.1088/1361-6501/aa4e9e.

[16] C.M. de Silva, E.P. Gnanamanickam, C. Atkinson, N.A. Buchmann, N. Hutchins, J. Soria, I. Marusic, High spatial range velocity measurements in a high Reynolds number turbulent boundary layer, Phys. Fluids 26 (2) (2014) 025117, http://dx.doi.org/10.1063/1.4866458.

[17] C. Willert, High-speed particle image velocimetry for the efficient measurement of turbulence statistics, Exp. Fluids 56 (1) (2015) 17, http://dx.doi.org/10.1007/s00348-014-1892-4.

[18] C.E. Willert, C. Cuvier, J.M. Foucaut, J. Klinner, M. Stanislas, J.P. Laval, S. Srinath, J. Soria, O. Amili, C. Atkinson, C.J. Kähler, S. Scharnowski, R. Hain, A. Schröder, R. Geisler, J. Agocs, A. Röse, Experimental evidence of near-wall reverse flow events in a zero pressure gradient turbulent boundary layer, Exp. Therm Fluid Sci. 91 (2018) 320–328, http://dx.doi.org/10.1016/j.expthermflusci.2017.10.033.

[19] P. Lenaers, Q. Li, G. Brethouwer, P. Schlatter, R. Örlü, Rare backflow and extreme wall-normal velocity fluctuations in near-wall turbulence, Phys. Fluids 24 (3) (2012) 035110, http://dx.doi.org/10.1063/1.3696304.

[20] J. Sheng, E. Malkiel, J. Katz, Using digital holographic microscopy for simultaneous measurements of 3d near wall velocity and wall shear stress in a turbulent boundary layer, Exp. Fluids 45 (6) (2008) 1023–1035, http://dx.doi.org/10.1007/s00348-008-0524-2.

[21] S.S. Kumar, X. Huang, X. Yang, J. Hong, Three dimensional flow motions in the viscous sublayer, Theor. Appl. Mech. Lett. 11 (2) (2021) 100239, http://dx.doi.org/10.1016/j.taml.2021.100239.

[22] T. Fuchs, C.J. Kähler, Single axis volumetric μPTV for wall shear stress estimation, in: Proceedings of the 13th International Symposium on Particle Image Velocimetry, 2019, URL https://athene-forschung.unibw.de/129386.

[23] S. Chen, N. Angarita-Jaimes, D. Angarita-Jaimes, B. Pelc, A.H. Greenaway, C.E. Towers, D. Lin, D.P. Towers, Wavefront sensing for three-component three-dimensional flow velocimetry in microfluidics, Exp. Fluids 47 (2009) 849, http://dx.doi.org/10.1007/s00348-009-0737-z.

[24] C. Cierpka, R. Segura, R. Hain, C.J. Kähler, A simple single camera 3C3D velocity measurement technique without errors due to depth of correlation and spatial averaging for microfluidics, Meas. Sci. Technol. 21 (4) (2010) 045401, http://dx.doi.org/10.1088/0957-0233/21/4/045401.

[25] R. Barnkob, M. Rossi, General defocusing particle tracking: fundamentals and uncertainty assessment, Exp. Fluids 61 (2020) 110, http://dx.doi.org/10.1007/s00348-020-2937-5.

[26] T. Fuchs, M. Bross, C.J. Kähler, Wall-shear-stress measurements using volumetric μPTV, Exp. Fluids 64 (6) (2023) 115, http://dx.doi.org/10.1007/s00348-023-03656-1.

[27] P.H. Alfredsson, R. Örlü, The diagnostic plot — a litmus test for wall bounded turbulence data, Eur. J. Mech. B Fluids 29 (6) (2010) 403–406, http://dx.doi.org/10.1016/j.euromechflu.2010.07.006.

[28] C. Willert, M. Gharib, Three-dimensional particle imaging with a single camera, Exp. Fluids 12 (6) (1992) 353–358, http://dx.doi.org/10.1007/BF00193880.

[29] F. Pereira, M. Gharib, D. Dabiri, D. Modarress, Defocusing digital particle image velocimetry: a 3-component 3-dimensional DPIV measurement technique. Application to bubbly flows, Exp. Fluids 29 (1) (2000) S078–S084, http://dx.doi.org/10.1007/s003480070010.

[30] F. Pereira, M. Gharib, Defocusing digital particle image velocimetry and the three-dimensional characterization of two-phase flows, Meas. Sci. Technol. 13 (5) (2002) 683, http://dx.doi.org/10.1088/0957-0233/13/5/305.

[31] S.Y. Yoon, K.C. Kim, 3D particle position and 3D velocity field measurement in a microvolume via the defocusing concept, Meas. Sci. Technol. 17 (11) (2006) 2897–2905, http://dx.doi.org/10.1088/0957-0233/17/11/006.

[32] F. Pereira, J. Lu, E. Castaño-Graff, G. M., Microscale 3d flow mapping with μDDPIV, Exp. Fluids 42 (2007) 589–599, http://dx.doi.org/10.1007/s00348-007-0267-5.

[33] J. Lu, F. Pereira, S.E. Fraser, M. Gharib, Three-dimensional real-time imaging of cardiac cell motions in living embryos, J. Biomed. Opt. 13 (1) (2008) 014006, http://dx.doi.org/10.1117/1.2830824.

[34] J. Klinner, C. Willert, Feasibility of multi-aperture micro-PTV for wall shear stress measurements, in: 20th International Symposium on Application of Laser and Imaging Techniques to Fluid Mechanics, 2022, http://dx.doi.org/10.55037/lxlaser.20th.167.

[35] C. Cierpka, S. Scharnowski, C.J. Kähler, Parallax correction for precise near-wall flow investigations using particle imaging, Appl. Opt. 52 (12) (2013) 2923–2931, http://dx.doi.org/10.1364/AO.52.002923, Publisher: Optica Publishing Group.

[36] C. Willert, J. Klinner, Dynamic wall shear stress measurement using event-based 3d particle tracking, Exp. Fluids (2025) http://dx.doi.org/10.1007/s00348-024-03946-2.

[37] N.A. Malik, T. Dracos, D.A. Papantoniou, Particle tracking velocimetry in three-dimensional flows, Exp. Fluids 15 (4) (1993) 279–294, http://dx.doi.org/10.1007/BF00223406.

[38] N.T. Ouellette, H. Xu, E. Bodenschatz, A quantitative study of three-dimensional Lagrangian particle tracking algorithms, Exp. Fluids 40 (2) (2006) 301–313, http://dx.doi.org/10.1007/s00348-005-0068-7.

[39] A. Fage, H.C.H. Townend, G.I. Taylor, An examination of turbulent flow with an ultramicroscope, Proc. R. Soc. Lond. Ser. A 135 (828) (1932) 656–677, http://dx.doi.org/10.1098/rspa.1932.0059, Publisher: Royal Society.

[40] L.H. Benedict, R.D. Gould, Towards better uncertainty estimates for turbulence statistics, Exp. Fluids 22 (2) (1996) 129–136, http://dx.doi.org/10.1007/s003480050030.

[41] M. Quadrio, P. Luchini, Integral space–time scales in turbulent wall flows, Phys. Fluids 15 (8) (2003) 2219–2227, http://dx.doi.org/10.1063/1.1586273.

[42] P.H. Alfredsson, R. Örlü, P. Schlatter, The viscous sublayer revisited–Exploiting self-similarity to determine the wall position and friction velocity, Exp. Fluids 51 (1) (2011) 271–280, http://dx.doi.org/10.1007/s00348-011-1048-8.

[43] Q. Chen, Y. Duan, Q. Zhong, Z. Wang, L. Huang, On the method of determining instantaneous wall shear stress from near-wall velocity measurements in wall turbulence, Phys. Fluids 33 (12) (2021) 125105, http://dx.doi.org/10.1063/5.0068077.

[44] P. Schlatter, R. Örlü, Assessment of direct numerical simulation data of turbulent boundary layers, J. Fluid Mech. 659 (2010) 116–126, http://dx.doi.org/10.1017/S0022112010003113, Publisher: Cambridge University Press.

[45] J. Jiménez, S. Hoyas, M.P. Simens, Y. Mizuno, Turbulent boundary layers and channels at moderate Reynolds numbers, J. Fluid Mech. 657 (2010) 335–360, http://dx.doi.org/10.1017/S0022112010001370.

[46] J.A. Sillero, J. Jiménez, R.D. Moser, One-point statistics for turbulent wall-bounded flows at Reynolds numbers up to $\delta^+ \approx 2000$, Phys. Fluids 25 (10) (2013) http://dx.doi.org/10.1063/1.4823831, Publisher: AIP Publishing.

[47] N. Hutchins, K.S. Choi, Accurate measurements of local skin friction coefficient using hot-wire anemometry, Prog. Aerosp. Sci. 38 (4) (2002) 421–446, http://dx.doi.org/10.1016/S0376-0421(02)00027-1.

[48] Z.W. Hu, C.L. Morfey, N.D. Sandham, Wall pressure and shear stress spectra from direct simulations of channel flow, AIAA J. 44 (7) (2006) 1541–1549, http://dx.doi.org/10.2514/1.17638, Publisher: American Institute of Aeronautics and Astronautics.

[49] M.P. Simens, J. Jiménez, S. Hoyas, Y. Mizuno, A high-resolution code for turbulent boundary layers, J. Comput. Phys. 228 (11) (2009) 4218–4231, http://dx.doi.org/10.1016/j.jcp.2009.02.031.

[50] R. Örlü, P. Schlatter, On the fluctuating wall-shear stress in zero pressure-gradient turbulent boundary layer flows, Phys. Fluids 23 (2) (2011) 021704, http://dx.doi.org/10.1063/1.3555191.

[51] G.K.E. Khoury, P. Schlatter, G. Brethouwer, A.V. Johansson, Turbulent pipe flow: Statistics, re-dependence, structures and similarities with channel and boundary layer flows, J. Phys. Conf. Ser. 506 (1) (2014) 012010, http://dx.doi.org/10.1088/1742-6596/506/1/012010.

[52] D. Schanz, S. Gesemann, A. Schröder, Shake-The-Box: Lagrangian particle tracking at high particle image densities, Exp. Fluids 57 (5) (2016) 70, http://dx.doi.org/10.1007/s00348-016-2157-1.

[53] A. Schröder, D. Schanz, R. Geisler, P. Godbersen, J. Agocs, A.R. Simhan, Near-wall flow features in ZPG-TBL at various Reynolds numbers using dense 3D Lagrangian particle tracking, in: 21st International Symposium on Application of Laser and Imaging Techniques to Fluid Mechanics, Lisbon, Portugal, 2024, http://dx.doi.org/10.55037/lxlaser.21st.226.

[54] G. Schröder, H. Treiber, Technische Optik: Grundlagen und Anwendungen, in: Kamprath-Reihe, Vogel, 2002.

[55] C. Willert, M. Novara, D. Schanz, R. Geisler, M. Schroll, S. Ribergard, A. Schröder, Multi-resolution, time-resolved PIV measurements of a decelerating turbulent boundary layer near separation, in: 14th International Symposium on Particle Image Velocimetry, Vol. 1, No. 1, 2021, http://dx.doi.org/10.18409/ispiv.v1i1.77.